Summer 2017

Study of Iron Ion Transit through Three-Fold Channel of Ferritin Cage

Shah Alam Limon
Missouri State University, ShahAlam722@live.missouristate.edu

STUDY OF IRON ION TRANSIT THROUGH THREE-FOLD CHANNEL OF FERRITIN CAGE

A Masters Thesis

Presented to

The Graduate College of

Missouri State University

In Partial Fulfillment

Of the Requirements for the Degree

Master of Science, Materials Science

By

Shah Alam Limon

August 2017

STUDY OF IRON ION TRANSIT THROUGH THREE-FOLD CHANNEL OF FERRITIN CAGE

Physics, Astronomy and Materials Science

Missouri State University, August 2017

Master of Science

Shah Alam Limon

ABSTRACT

Ferritin is an iron-storage globular protein with an ability to uptake, mineralize and release iron ions in a controllable manner. The globular hollow shell allows storage of mineralized iron, with several channels responsible for the transit of ions into the shell and out of it. Understanding of the detailed molecular functioning of ferritin is required for rational design of biomimetic conjugate nano-biosystems containing ferritin-like constituents. In this work, ferritin was investigated both numerically by all-atom molecular dynamics (MD) simulations, and experimentally by Raman spectroscopy. Molecular dynamic simulations of a model system comprising iron ions (Fe^{2+}) and a ferritin trimer expressing a three-fold channel responsible for the ion transport, have revealed a quick entering of ions in the channel. The transit of iron ions through the channel was thoroughly investigated. The transit was found to be driven by both electrostatic charge of ferritin, and interaction between the ions. Exit (expulsion) of an iron ion from the channel was observed at a condition that at least one more ion is present in the channel. Raman characterization of an iron-loaded ferritin solution revealed pronounced bands attributable to iron, as expected. However, Raman spectra of apo-ferritin, which does not contain an iron mineral, also exhibited similar bands. Based on the results of MD simulations, it was hypothesized that apo-ferritin retains iron ions in its three-fold channels, and these ions may produce the observed Raman bands. The study of molecular mechanisms involved in the iron ion transit elucidates the pathways of iron uptake and release in ferritin.

KEYWORDS: ferritin, iron ion transit, molecular dynamics, Raman spectroscopy, nano-biological conjugation

This abstract is approved as to form and content

_____

Maria Stepanova, PhD
Chairperson, Advisory Committee
Missouri State University

STUDY OF IRON ION TRANSIT THROUGH THREE-FOLD

CHANNEL OF FERRITIN CAGE

By

Shah Alam Limon

A Masters Thesis
Submitted to the Graduate College
Of Missouri State University
In Partial Fulfillment of the Requirements
For the Degree of Master of Science, Materials Science

August 2017

Approved:

_____
Maria Stepanova, PhD

_____
Kartik Ghosh, PhD

_____
Matthew Siebert, PhD

_____
Julie Masterson, PhD: Dean, Graduate College

ACKNOWLEDGEMENTS

I am very thankful to the Department of Physics, Astronomy and Materials Science of Missouri State University for providing enormous facilities to complete my graduate studies here. I am thankful to my research supervisor Dr. Maria Stepanova for continuously helping me learn about experimental and molecular dynamics simulation techniques. Special thanks to my academic advisor and thesis committee member Dr. Kartik Ghosh, who inspired me in achieving success, helped me in academic affairs and guided me in the right direction whenever needed. I am grateful to Dr. Matthew Siebert, for being the thesis committee member. I also want to thank Dr. Mayanovic, Dr. Plavchan and Dr. Sakidja for allowing me to use different experimental and computational resources.

As an international student here at MSU, it has been a great privilege for me to have wonderful host families: Nancy & Kent Parrish, Twyla & Bob McGurty, Susan & Mike Burton, and Suzanne & Ted Lennard. I am thankful to them for sharing American culture with me and making my time here in Springfield, MO very much fantastic. Fellow graduate students Delower, Harsha, Shaolin, Paul, Bithi, Reaz, Samiul, Austin, and Dan helped me in my research work in different ways, and I am grateful to them.

Last but not least, I am thanking my parents, Dr. Liakat Ali and Ms. Dalia Shirin, my sister Shabnam, and my wife Anahita for supporting me always.

TABLE OF CONTENTS

LIST OF TABLES

LIST OF FIGURES

CHAPTER 1: INTRODUCTION

The work described here is dedicated to computational and experimental studies of ferritin, a cage protein involved in iron ion storage and release processes. Applications of ferritin include rational design of biomimetic conjugate nano-biosystems, synthesizing nanodot arrays, protein crystallization to form nano-porous membranes, transport of drug delivery agents, and many others.

In this work, all-atom molecular dynamics simulations of a fragment of ferritin cage are done in order to better understand detailed functioning of ferritin. The fragment considered expresses a three-fold channel, which is responsible for transport of iron ions in and out of ferritin globule. The molecular dynamics procedures, including energy minimization, equilibration, and production simulations were done using the GROMACS molecular dynamics package. Transit of iron ions through the three-fold channel was thoroughly analyzed.

In experimental studies of ferritin, Raman spectroscopy was used. The advantage of Raman spectroscopy is that it allows capturing unique vibrational fingerprints of molecules. In this work, Raman spectra of iron-loaded ferritin solution were collected. Raman spectra of apo-ferritin were also acquired. Colloidal Au nanoparticles were employed in one of the experimental setups in order to achieve surface enhanced Raman scattering of ferritin samples. Results of Raman characterization of the various samples of ferritin were interpreted in light of molecular mechanisms revealed by the computational studies.

CHAPTER 2: LITERATURE REVIEW

2.1. Biotic and Abiotic Nanomaterials

Conventionally the term "nano" is attributed to an object of 100 nm dimensions or below. Nevertheless, FDA and IUPAC suggest that any particle under one micrometer with dimension-dependent property could be identified as a nanoparticle.[1] The conjugation of abiotic nanostructures with nanostructured biological species has significant applications in various areas including drug delivery systems, bioimaging, nanofabrication, bioenergy and biofuels, medicine, and biomimetic conjugate nano-bio systems. The key aspect of both naturally occurring and processed biotic materials is their biocompatibility inside living organisms. Abiotic nanostructures, in turn, act as a constituent for characterization of biomolecules. For instance, Au and Ag nanoparticles can greatly enhance the Raman scattering of biomolecules, a technique known as Surface Enhanced Raman Spectroscopy (SERS) [2,3].

Nanoparticles can be found in nature or they can be synthesized artificially. Natural nanoparticles are a result of natural phenomena, such as volcanic eruption or forest fire [4,5]. Synthesized nanoparticles can be prepared in different ways, such as hydrothermal synthesis, gas condensation, chemical vapor deposition, dispersion in solvent, synthesis by colloidal techniques, etc.[6,7] Nucleation and growth processes play a key role in nanoparticle synthesis[6]. Synthesized nanoparticles have tremendous applications facilitated by their physical properties. One of the important applications is detection of proteins and DNA[5].

While discussing biotic- abiotic nanostructures, one of the most important criteria would be size requirements. One of the aspects is size compatibility between

nanoparticles and biological species. To understand intra and inter cellular mechanisms, which is important to interpret many functions of biological species, size compatibility would be a significant factor. Average cell size of bio-organisms is approximately 10 μm. The cell constituents are in a nm range; for instance, protein size is typically less than 100 nm. Incorporating nanoparticles of similar size as a probe is a promising technique to understand cell mechanisms at a molecular level.

There is a wide range of applications for nanomaterials in biological sciences, such as fluorescent tags for bio-detection, protein characterization, drug delivery, DNA probing, enhancement of MRI contrast agents, or cancer cell detection.[8] Besides the size compatibility, interactions between nanoparticles and biomolecules are also important. One interacting media is coating - for example, a biopolymeric coating that acts as binding agent between biological and inorganic surfaces.

2.2 Raman and Surface Enhanced Raman Spectroscopy

Raman spectroscopy is a versatile non-destructive characterization technique involving an extraordinary phenomenon called Raman scattering. It involves inelastic scattering of photons from a molecule upon exposure to light. Raman spectra are representative of vibrational characteristics of a material. Since Raman spectroscopy can detect different modes of molecular vibrations, it shows unique vibrational fingerprints of many materials including crystalline solids, non-crystalline solids, biological species, liquids, thin films, etc. Raman effect was discovered by C.V. Raman in 1928, for which he received his Nobel prize in 1930. Since then Raman spectroscopy is such a broadly

used characterization technique, that the Raman effect was granted the status of National Historic Chemical Landmarks by American Chemical Society in 1998[9].

The Raman scattering is an inelastic scattering of light by materials. Various types of light scattering are shown in Figure 2.1. These include:

- Rayleigh scattering (elastic)
- Stokes Raman scattering (inelastic)
- Anti- Stokes Raman scattering (inelastic) .
- Fluorescence (inelastic)

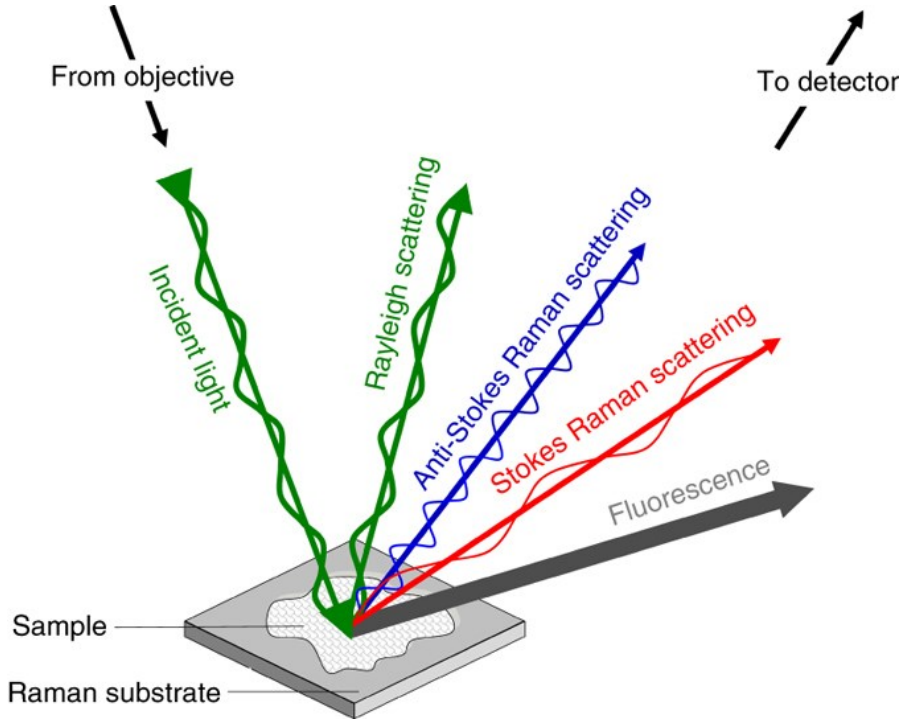

Figure 2.1: Raman scattering types. Adapted with permission from Ref. 10.

The diagram in Figure 2.2 explains the difference between some of these scattering processes. Rayleigh scattering is elastic scattering, such that the same

wavelength is reflected as of the incident beam. In contrast, Stokes Raman scattering has a longer wavelength of scattered light than the incident beam, and anti-Stokes scattering has a shorter wavelength. The Raman shift is the difference between the incident and reflected wavenumbers. Raman spectra may comprise both Stokes and anti-Stokes Raman scattering, with the exclusion of Rayleigh scattering. Fluorescence is a different inelastic emission phenomenon resulting from absorption of light. When an atom relaxes from an exited energy state to ground state, the energy is released as a photon, which constitutes fluorescence. In distinction from narrow Raman bands, fluorescence produces a broad background in the spectra.

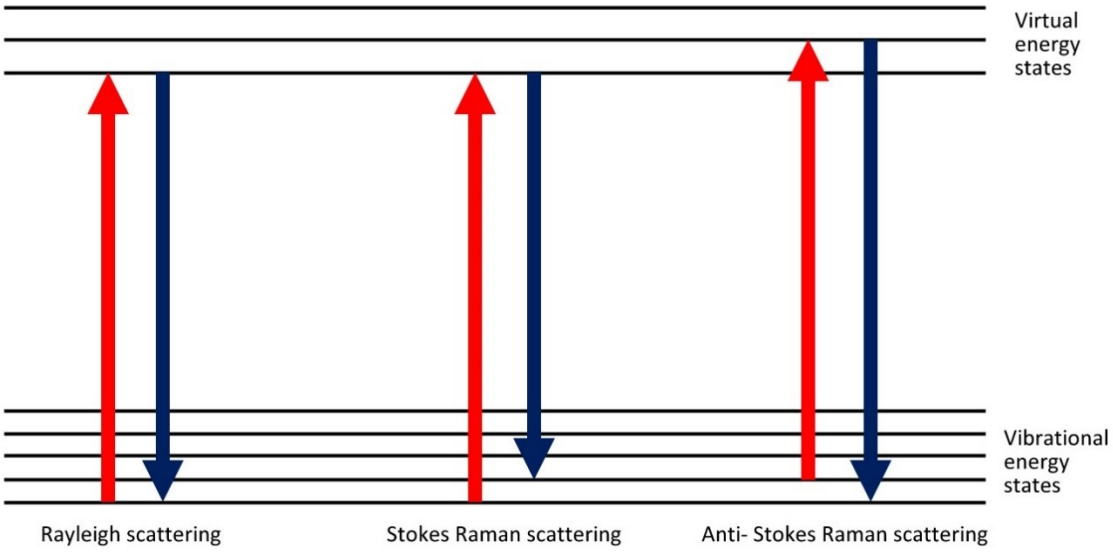

Figure 2.2: Energy level diagram for Raman and Rayleigh scattering.

When nano sized metallic species are incorporated in a sample, the Raman scattering is enhanced. This phenomenon is known as Surface Enhanced Raman

Scattering (SERS). The mechanism of surface enhanced Raman scattering is not yet fully understood. The enhancement can be explained electromagnetically, based on localized surface plasmon resonance (LSPR). Localized surface plasmons are oscillations of conduction electron system in metal nanostructures, which are smaller in comparison with incident light's wavelength.[11] When light incidents upon such metal nanostructures, this results in excitation of surface plasmons. Maximum excitation happens when plasmonic frequency is in resonance with incoming beam frequency. It is analogous with constructive interference. The incident light excites the electron cloud resulting in LSPR. Excitation of LSPR in metal nanostructures contributes to a buildup of local electromagnetic field around the nanostructures, creating so called hot spots. Raman scattering of light occurring in the area of a hot spot is significantly enhanced. Thus, hot spots are the SERS enhancement sites. Raman scattering by molecules will experience an enhancement when that molecule is in close proximity of a hot spot. Silver and gold nanoparticles are particularly efficient as LSPR active nanostructures. Since Raman spectroscopy may have orders of magnitude smaller scattering cross section than fluorescence cross section[12], the enhancement is important for sensitivity of Raman characterization.

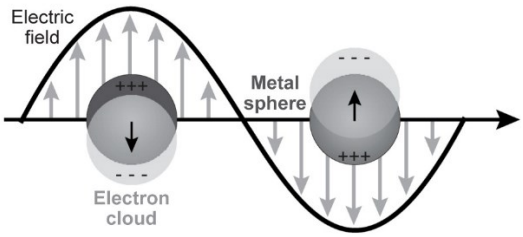

Figure 2.3: Scheme of Localized Surface Plasmon Resonance excitation by incident monochromatic light. Reproduced with permission from Ref. 13.

The strongest hot spots are created when two or more neighboring nanoparticles are at a distance of several nanometers[14,15]. Possible ways to obtain hot spots are reviewed in many publications, for example by Xu et al.[16] This may include adding aggregation agents[17], heat enabled self- assembly[18], or hydrophobicity driven aggregation[19].

Two types of SERS applications can be distinguished - intrinsic and extrinsic[16,20]. Intrinsic SERS is a direct acquisition of Raman spectra that represents inherent vibrational signatures of biomolecules. Intrinsic SERS is also known as label-free detection of biomolecules. This label-free detection enables direct characterization of sample molecules. The examples include detection of glucose[21,22], antioxidants[23], amino acids[24], proteins[16] and DNA[25]. Extrinsic or labeled SERS detection is an indirect way of detection where a Raman-active label or probing particle is attached to sample molecules, and Raman spectra are obtained from the probing particle, not the molecules Thus, it is an indirect way of characterizing the system. Extrinsic SERS applications involve characterization of living cells[26], including cancer cells[27].

2.3 SERS of Biological Samples

In recent years Raman spectroscopy and SERS have been widely used for bio-detection[12,28–31]. SERS enables label free chemical quantification of materials[16,32]. Wide range of biomolecules such as proteins, lipids, or nucleic acids have been successfully detected by SERS technique in recent years[33,34]. Being a non-destructive technique, SERS also provides an opportunity of avoiding cumbersome sample preparation techniques or performing complex chemical reactions. Portable SERS detectors can be used to detect chemical and biological hazards and contaminants[32].

Most noteworthy for biological materials characterization by SERS is the capability of attaining Raman spectra from nano-sized volumes. Especially single molecule Raman characterization capability makes SERS unique for biodetection[13,32]. In comparison with using fluorescent tags for bio-characterization, SERS is much more efficient than fluorescent tags. SERS provides vibrational information specific to molecules, that fluorescence cannot capture.

The SERS method usually involves a usage of LSPR active noble metal components such as Au or Ag. Such SERS substrates play a crucial role in signal enhancement. For example, a layer of colloidal Au or Ag nanoparticles of size ranging from 10 nm to 100 nm is a good surface enhancer[12]. Besides, there are examples of using salts with SERS active sites for surface enhancement agent[35]. Examples of Ag ion clusters with iodide complex ions acting as a SERS active surface can be found in the literature[36,37]. Evaporated films of Au or Ag or nanostructures of these metals also provide SERS enhancement. In one of SERS applications, Au or Ag electrodes are used to study biological processes[19].

In most cases, evaporated films and colloidal nanostructures of Au and Ag have a larger enhancement than bulk electrodes. The significance of SERS active electrodes is the possibility to vary the surface potential, which can be used to study charge transfer mechanism between target molecules and metal surface.

SERS substrates for biological materials should meet certain requirements of size and shape, and also be compatible with the biomolecules. As a noble metal, gold is inert against most chemical species, which is a valuable property for SERS biodetection. Generally, silver is a stronger enhancer than Au, however it oxidizes quickly, for which reason gold nanoparticles are more suitable for SERS biodetection[38].

Numerous examples of Raman and SERS biodetection can be presented. For example, SERS allows detecting fragments of DNA, along with identification of individual bases Adenine, Guanine, Cytosine, or Thymine[39].

Raman or SERS characterization can be performed on entire living cells[12,40,41]. Drug delivery within the cell and drug- nucleic acid complex have been characterized by SERS technique with silver nanoparticles[12]. Moreover, SERS mapping can reveal inhomogeneous structure of the cell, detailing nucleus and cytoplasm constituents by respective bands. The cells remained alive after SERS experiments[12] and showed all functional characteristics. Thus, structural morphology of single cell can be evaluated by SERS technique. This may facilitate probing of chemical changes in the cell, which may result in a physiological impact. An important application involves detecting cancer cells' physio-chemical characteristics in order to rationally combat cancer diseases.

Raman and SERS detection of proteins is particularly important[17,33,34,42,43]. As stated before, label free or intrinsic SERS characterization gives vibrational

characteristics of the sample biomolecule directly. For proteins, this label free detection has been widely used in recent years[16]. Important advantages of intrinsic SERS detection of proteins are the sensitivity and specificity of the spectra. Sensitivity of SERS depends on morphology of the surface of metal nanoparticles. Designing NPs with more "hot spots"[16] allows a higher probability of finding proteins close to hot spots, which enables a more sensitive detection. However, a challenge involves reproducibility of SERS spectra from experiment to experiment. Variability in Raman spectra of same protein from different experiments may be attributed to interfacial properties of nanoparticles, adsorption orientation or laser induced reactions[16]. Reproducibility of Raman and SERS spectra is a challenge. It was found that[44] DNA covered Au nanoparticles form nanobridged Au structures which can produce uniform and reproducible SERS spectra. Improved reproducibility of SERS spectra of a protein in aqueous solution due to weakening of laser-induced reaction has been reported[17]. Whether the protein remains in its native state or not during Raman experiments is another much addressed point. Sometimes, SERS and Raman spectra are somewhat different.

Proteins in aqueous media retain their native state, as inside living organism proteins are always in solution. If immersed in proper aqueous media, proteins would be representative of their native conditions. SERS spectra taken on dry protein may result in somewhat different Raman bands. Also, protein vibrations may experience a change as a result of binding with metal NPs[45]. The general knowledge is that it is better to take Raman or SERS spectra of proteins in a liquid[45]. Also, in aqueous solution, SERS can be used to detect protein's conformational changes.

2.4 Molecular Dynamics Simulations

Molecular dynamics (MD) simulation is a classical N-body simulation, which represents processes in molecular systems, by solving Newton's equations of motion. Numerical solution of Newton's equations of motion generates a sequence of snapshots, representing positions of all atoms in a molecule at selected moments of time. Forces between the atoms and their potential energy are calculated using classical interatomic potentials. A potential that determines the functional of potential energy with respect to distance is central for molecular dynamics simulations. In MD applications, this energy information is known as the force field.

MD simulations can provide a detailed representation of molecular movements, which can predict or explain mechanisms of physical and chemical processes such as diffusion, mechanical properties, protein folding, molecular level morphologies, etc. Especially in molecular biology, modeling and simulations are of particular interest as many biological processes are difficult to study experimentally in molecular detail. Molecular dynamics studies are widely used in theoretical physics, materials science, biophysics, physical chemistry, molecular biology, electrical engineering, mechanical engineering, and materials science - in almost all fields of science and technology.[46–53] Emphasis on biomolecules will be done in my current work.

Examples of MD simulations in biological materials include protein 3D structure refinement that is obtained from XRD or NMR spectroscopy, biophysical process analysis by MD simulation of macromolecular species (proteins or nucleic acids) movement, drug delivery mechanisms, diffusion of atoms in fuel cells, motion of dopant atoms in crystals, motor protein transport, study of protein- ligand complexes,[46–51,54] etc.

As MD simulations can express positions of atoms as a function of time, it is very useful to interpret properties of molecular systems. Biophysical phenomena are the best examples.

Clearly, computational models used in MD may have limitations. Experimental techniques can be employed to check the validity of numerical predictions. Comparison between experimental and simulation results either confirms the findings, or serves to improvement of simulation protocols[50,55].

As the potential, or force field, is a key aspect of MD simulations, defining an approximation of forces between interacting atoms is one of the first steps in MD protocols. The potentials are editable, i.e. user can change various parameters of the potential, or force field, according to the needs of the system under consideration. Outcome of the simulations are accessible by visual software and images of molecular structure; video of simulation process and data analysis of parameters are the medium of interpretation of a computational study[56].

Karplus et al. suggested three types of applications[57] of molecular dynamics in mesoscopic systems. The first one is determining or refining of structure of a system with experimentally known parameters using MD. Second usage is describing the system at equilibrium. The properties that simulation describes are primarily structural and statistical-mechanical properties. The third application is interpreting the actual dynamics of a system where particle motion with time is described. First two types can conceivably be done by kinetic Monte Carlo simulations, whereas the third application is only possible with an MD simulation.

Molecular dynamics simulations for biological materials are made possible by very powerful and fast computers now-a-days, which enable working with thousands of atoms, whereas in early days such simulations were limited to a few hundred or even less atoms. Multiple simulations can be done in parallel to achieve a reliable statistics. There are many software packages available to simulate not only biological systems, but also many other complex systems; such as CHARMM, AMBER, GROMACS, NAMD, YASARA etc.

To understand protein behavior, molecular dynamics is a very efficient tool. As a protein is a dynamic system that experiences changes of conformations with time, vibrations of proteins are an interesting subject to investigate. Classical MD can predict and interpret protein's dynamic motion. Such detailed molecular-level analysis is difficult to do experimentally[58]. Furthermore, the interaction of protein with solvent and ions is also possible to represent by molecular dynamics simulations. MD simulation can interpret the solvent dynamics by analyzing motion of individual molecules or ions. The mechanisms of protein dynamics puzzled scientists for decades. By combining experimental and simulation techniques, it is now possible to understand dynamical properties of proteins in details.

2.5. Ferritin and Other Cage Proteins

Ferritin is an intracellular globular cage protein that is found in almost all living cells. Ferritin consists of 24 sub-units or monomers[59–61]. Each monomer has four large α-helices and a also a shorter helix, as shown in Figure 2.4. The monomers self-assemble in a 4-3-2 symmetric fashion[62]. In living cells, ferritin works as an iron storage protein[59–61]

being able to uptake, mineralize and release iron in a controllable manner. Ferritin stores iron in a form of mineral known as ferrihydrite inside its hollow space. When there is a deficiency of iron in the cell, ferritin releases iron, and when there is abundance of iron, ferritin stores extra iron in it. Figure 2.5 shows stored iron mineral cluster inside of a globule.

The atomic mass of horse ferritin is 440 kDa. It can store up to 4500 iron ions inside it in the mineralized form. The inside diameter of ferritin's shell is 8 nm and outside diameter is 12 nm. The shell is approximately 2 nm thick.

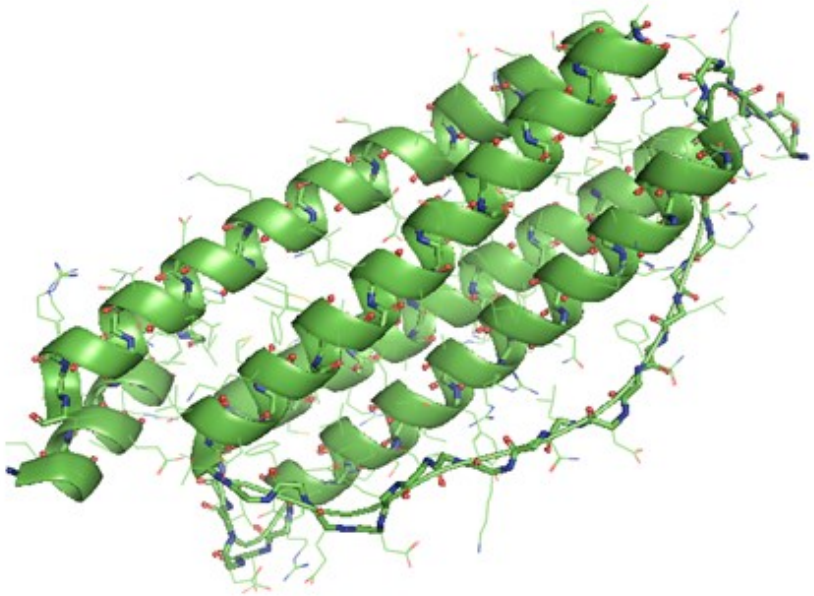

Figure 2.4: Ferritin monomer, PDB ID 5CZU.[63] The image was generated using PYMOL[64].

As ferritin consists of 24 monomers, there are three possible structural features on ferritin surface. They are known as two-fold symmetric junction, three-fold symmetric junction, and four-fold symmetric junction[65]. The three and four fold channels form funnel-like passageways[59] that connect interior space with exterior surroundings of the

protein, as shown in Figure 2.6. The three-fold channels are hydrophilic in nature, thus having the ability of passing ions and water molecules, whereas four-fold channels are hydrophobic, and therefore less efficient in passing charge-bearing species[59–61].

The technological significance of ferritin is that it is regarded as an important constituent for rational design of biomimetic conjugated nano-bio systems. As iron ions

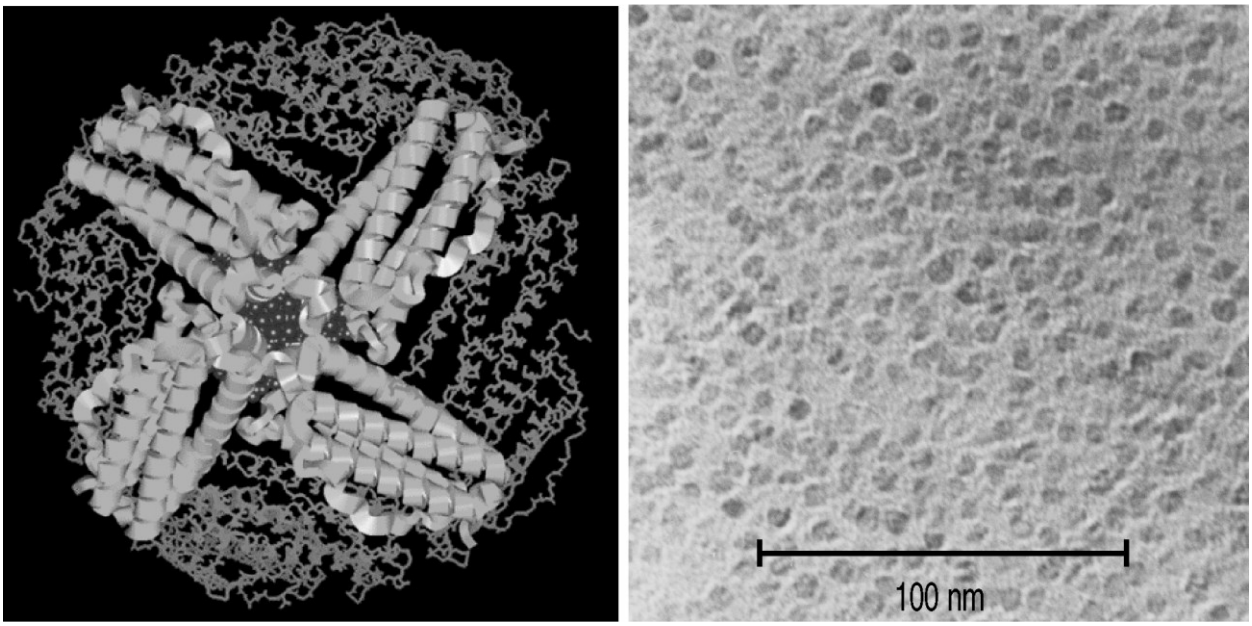

Figure 2.5: Ferrihydrite mineral inside ferritin cage and SEM image of iron loaded ferritin. Reproduced with permission from Ref. [66].

inside ferritin are stored as ferrihydrite minerals, fully loaded ferritin can work as a superparamagnetic nanoparticle[62]. Furthermore, as the ferritin cage has a definite size and shape, the cavity can incorporate inorganic particles of specific size, making possible synthesizing nanodot arrays inside the cage[65] as Figure 2.7 shows. This way, ferritin can be used as a template for nanostructure synthesis. The size and shape of nanoparticles influence electrical, magnetic, optical and other properties. Fabrication process involving

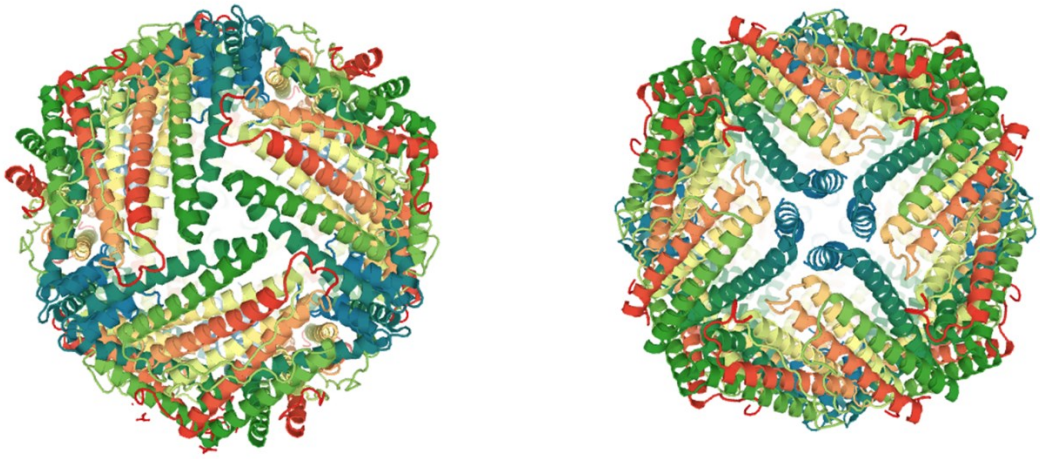

Figure 2.6: Ferritin's 3-fold channel (left) and 4-fold structure (right), PDB ID 5CZU. The image was generated using JMol[67].

ferritin can ensure a uniformity of structure-dependent properties. Many nanoparticles such as Au, Ag, Pt, Co, Cr, and Zn have already been successfully synthesized utilizing ferritin-like cavities[59,68–70]. Crystallized ferritin-like proteins can also act as a membrane, as the channels can pass ions, atoms, or small nanoparticles[65]. Ferritin is the most abundant member of the ferritin superfamily. However, there are many other ferritin-like cage proteins. The interior hollow space of cage proteins may carry various inorganic particles, thus making cage proteins a suitable template for nanoparticle synthesis[71–74].

Perhaps one of the most promising utilizations of cage proteins is in drug delivery[75]. Several advantages enable efficient drug delivery using protein cages. Nanoparticles are used for drug delivery because of their unique properties related to small size and surface morphology[31,75–77]. A narrow size distribution of NPs allows uniform drug dosing[75]. However, conventional NPs have some limitations, such as occasionally wide size distribution, low rate of drug transfer and sometimes instable

structure. Caged proteins encapsulating nanoparticles overcome some of these difficulties[31,75,78–80].

Caged proteins are formed by self-assembly of monomers into hollow spherical globules with uniform interior size. A protein cage may form by monomers of a single protein, such as ferritin; or by monomers of multiple proteins, for example cowpea mosaic virus (CPMV)[81]. Since protein cages have evolved in vivo, their utilization would involve primarily a selection of functional drug materials to be bonded in three distinct regions: interior surface, exterior surface, or inter-monomeric interfaces[75,79]. Control over functioning of cage proteins facilitates attaining a more efficient drug encapsulation. Also, by knowing detailed molecular structure and function of the cage channels, it is possible to control the amount of drug released, and its position in cage proteins[82].

2.6. Goals And Objectives Of The Work

The main goal of the work is to improve understanding of structure, dynamics, and function of ferritin at the molecular level. Specific objectives include the following:

- Performing all-atom molecular dynamic simulations of the interaction of iron ions with a model of three-fold channel of ferritin responsible for ions' transport;
- Analysis of molecular details relevant to transport of the ions through the channel in ferritin;
- Characterization of vibrational properties of iron-loaded ferritin and apo-ferritin using Raman spectroscopy;
- Comparative analysis of Raman bands of the different ferritin samples, and interpretation of the results in light of findings of the computational studies;
- Proof-of-principle SERS characterization of ferritin using colloidal gold nanoparticles for enhancement of Raman signal.

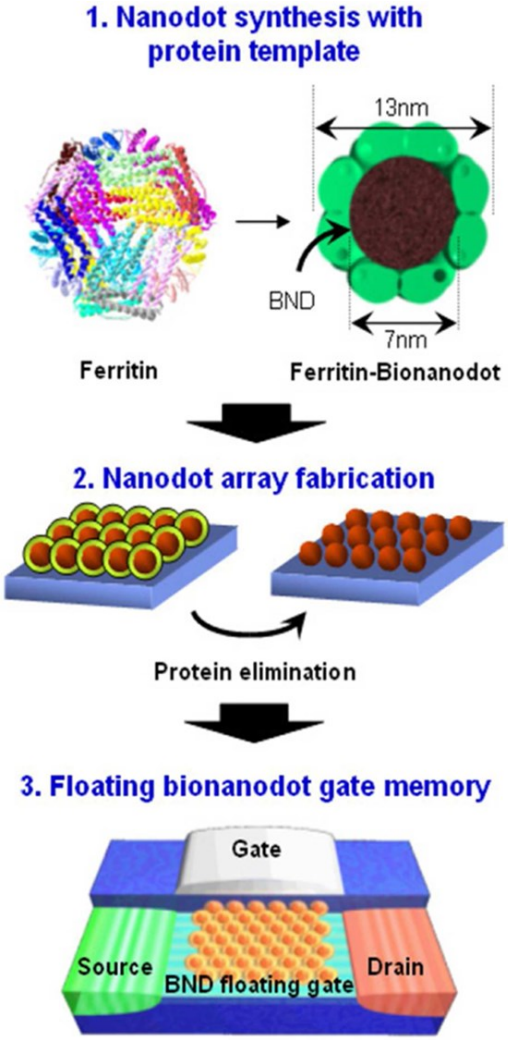

Figure 2. 7: Nanodot synthesis using ferritin as a template. Reproduced with permission from Ref. [65] .

CHAPTER 3: EXPERIMENTAL METHODS

3.1. LabRAM HR 800 Evolution Raman Spectroscope

In my work, the Raman characterization was done with Horiba LabRAM HR 800 Evolution Raman spectroscope. A 532 nm green laser was used for the excitation, and the Stokes scattering was received with edge filter. Among the various types of scattering, the LabRAM HR Evolution instrument can detect both Stokes and anti-Stokes Raman scattering, and also fluorescence background. Elastic Rayleigh scattering is blocked by an Edge filter. Stokes Raman scattering has higher wavelength than the incident beam, and anti-Stokes scattering has lower wavelength. Band-pass filter of Raman spectroscope passes only certain wavelengths and absorbs other wavelengths. Edge filter can pass the Stokes Raman scattering, and notch filter can pass both Stokes and anti-Stokes Raman scattering. Since in my experiment I used edge filter, only Stokes scattering was detected.

The characterization parameters were optimized for Raman characterization of liquid samples. Using a 10X microscopic lens facilitated proper focusing of the sample. A 10 seconds exposure time enabled the laser excitation of the samples. Upon rejection of elastically scattered light by the edge filter, the light passed through a 300 μm diameter confocal pinhole upon entering the spectrometer. The Horiba LabRAM 800 Evolution Raman spectroscope used in my work is shown in Figure 3.1, and a schematic diagram of Raman spectroscopic technique is shown in Figure 3.2.

Figure 3.1: Horiba LabRAM HR 800 Evolution Raman spectrometer.

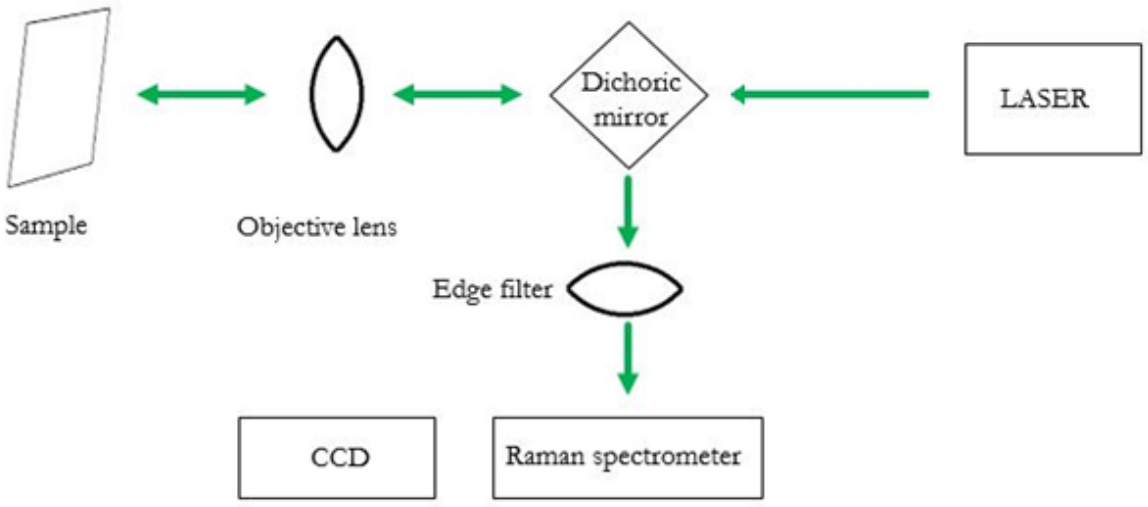

Figure 3. 2: Schematic diagram of Raman spectroscope.

3.2. Sample Preparation

The samples in my experimental work involve liquid solution of iron-loaded ferritin, lyophilized apo-ferritin powder, and ammonium iron (II) sulfate, or Mohr's salt. All these components were purchased from Sigma-Aldrich. The liquid sample contained purified ferritin from horse spleen in a 0.15 M saline solution (Sigma-Aldrich product no. F4503), dark red to brown in color. Total molecular weight of this ferritin is 440 kDa. According to supplier's specifications, the concentration of ferritin in the solution was under 125 mg/mL. The solution has been stored at temperature of 4-7 °C.

The lyophilized powdered apo-ferritin was also purified from horse spleen (Sigma-Aldrich product no 178440). The powder might contain 0.01% or less of iron. The powder was kept refrigerated. According to the supplier's specification, apo-ferritin is soluble in water or buffers up to a concentration of 1 mg/mL.

Ammonium iron (II) sulfate hexahydrate, also known as the Mohr's salt, has a chemical formula $(NH_4)_2Fe(SO_4)_2 \cdot 6H_2O$ and molecular weight of 392.14 g/mol (Sigma Aldrich product no. 203505). The salt is in crystalline powder form colored light blue. Mohr's salt is a common source of iron ions in lab experiments. Figure 3.3 shows these samples.

SERS of ferritin was enabled by surface enhancement with colloidal Au nanoparticles. 80 nm sized, citrate-stabilized Au nanoparticles in an 0.1 mM phosphate buffered saline (PBS) solution were purchased from Cytodiagnostics (GRF-80-20). Concentration of nanoparticles in the solution was 0.05 mg/mL. According to the specifications, individual Au nanoparticle's average volume was 2.68×10^5 nm^3, and their average surface area was 2.01×10^4 nm^2. However, my SEM characterization has

indicated that Au nanoparticles tended to aggregate with each other. As the SEM image in Figure 3.4 shows, some of the nanoparticles have coalesced into aggregates up to an approximately 350 nm size.

A B C

Figure 3.3: Samples of (A) liquid ferritin, (B) solid powdered ferritin, and (C) Mohr's salt.

Figure 3.5. shows a typical set up for liquid sample characterization in Raman spectroscope, with a droplet of liquid on a substrate. Au coated glass slides and silicon wafers were used as the substrates. Au coatings on glass slides were prepared by JVIC staff using magnetron deposition technique, with a thickness of the coating of 10 nm.

Several methods were implemented in my work to obtain the best Raman characterization of my samples. In one setup, a ferritin solution droplet was deposited on the substrate as illustrated in Figure 3.6. The lyophilized ferritin powder was either placed on a substrate and characterized directly, or powder ferritin was dissolved in HPLC water and subjected to Raman characterization from the solution. In some experiments, I did incubation of powder ferritin samples in water in a Petri dish for about

18 hours. Figure 3.7 shows the schematic of a Petri dish cross section. A two-compartment Petri dish is an ideal setup for incubation. One compartment contained DI water to maintain humid environment. The other compartment contained a substrate with liquid droplet on it. Humid atmosphere prevented the liquid of evaporation during the incubation.

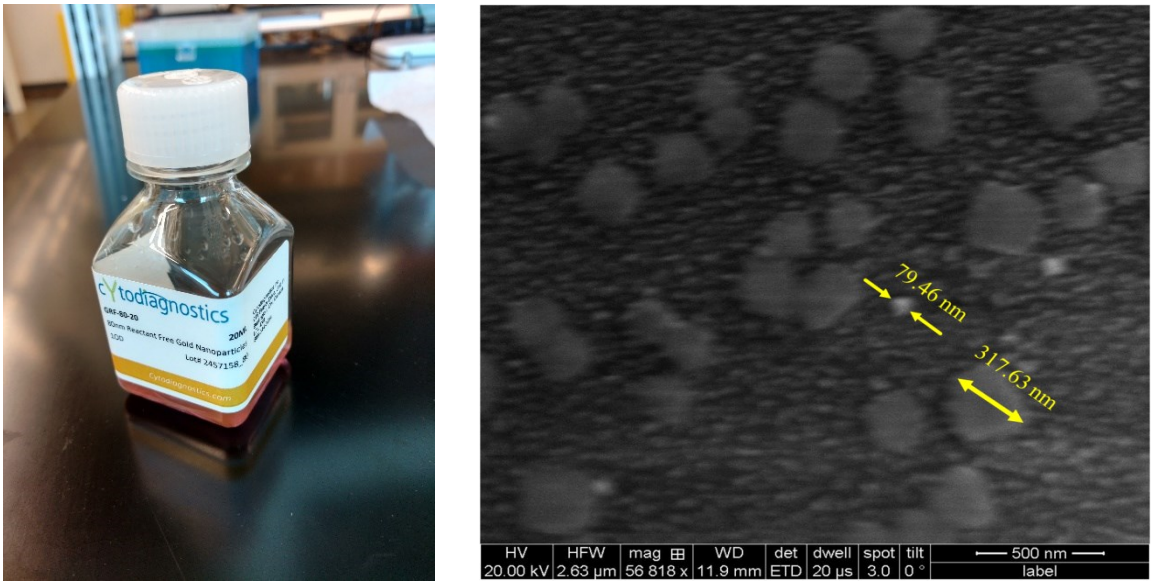

A B

Figure 3.4: 80 nm Au nanoparticles in PBS solution, and SEM image of the deposited Au NPs on PBS solution on a 10 nm Au coated glass substrate.

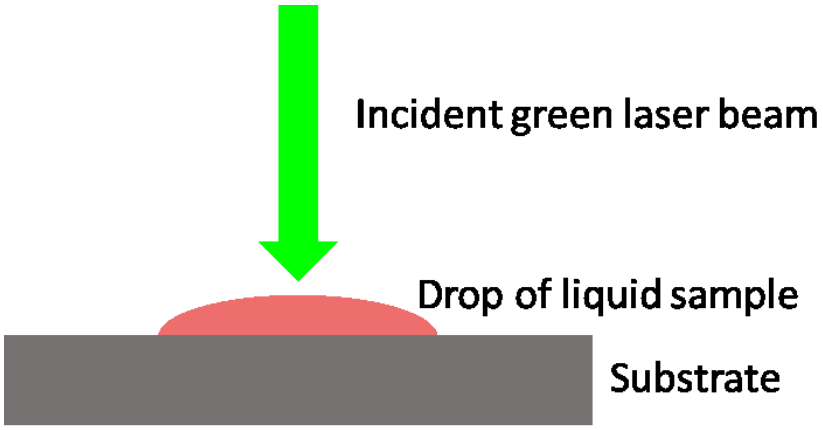

Figure 3.5: Experimental setup for liquid sample Raman characterization.

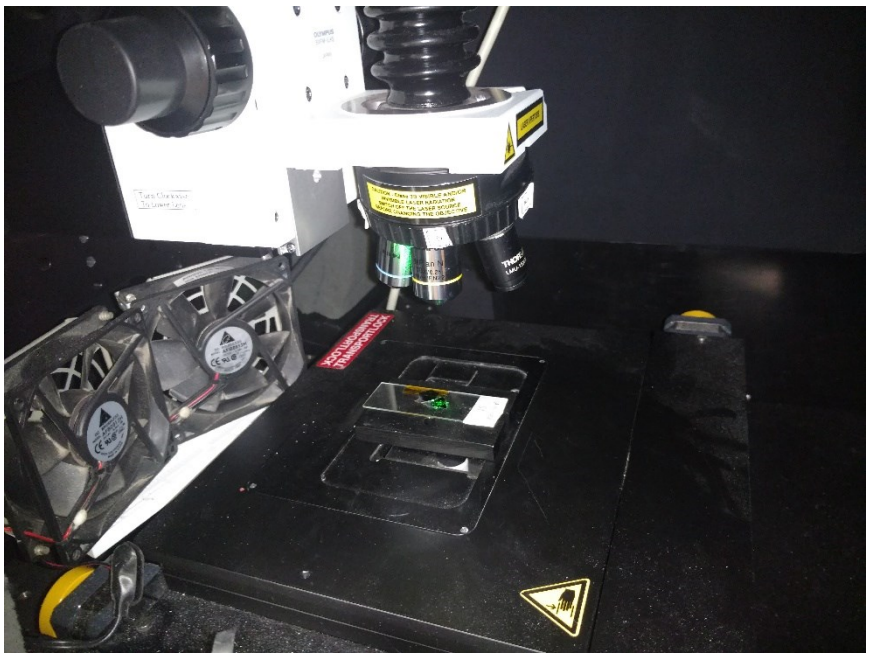

Figure 3.6: Raman spectroscopy setup showing incident laser on sample on a substrate.

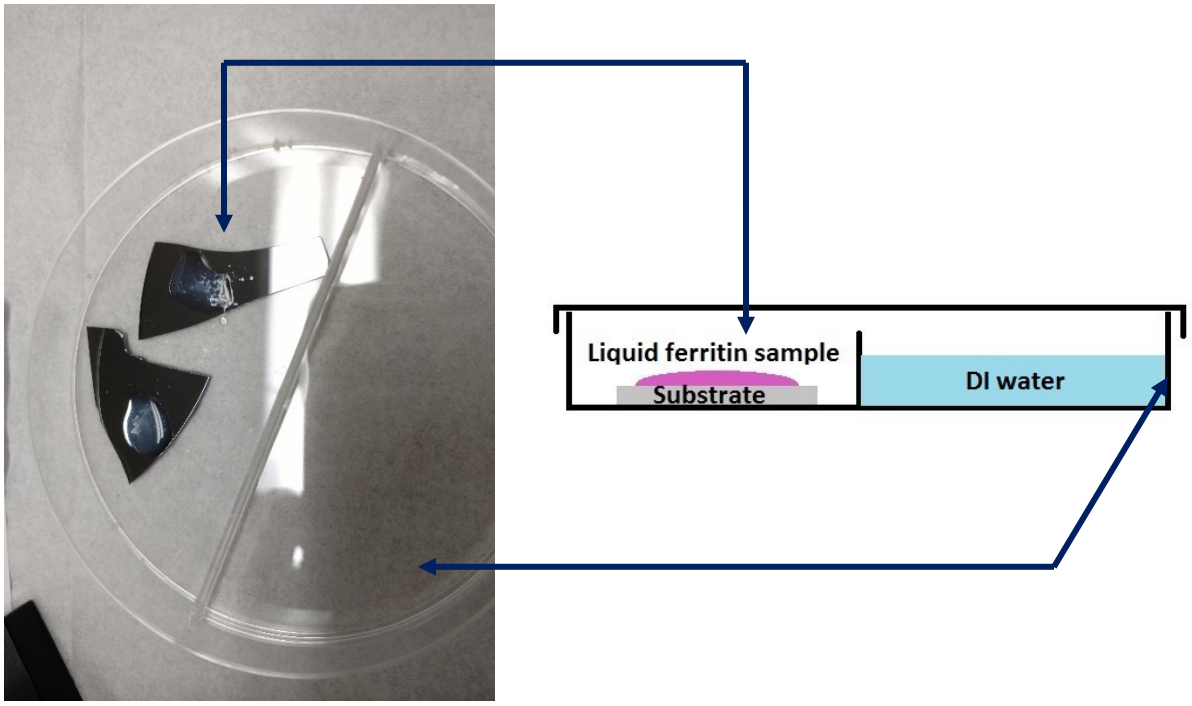

Figure 3.7: Incubation setup and cross-sectional schematic of a Petri dish with a sample.

3.3. Acquisition Of Raman Spectra

Calibration of Raman spectra is an important phase of the experiment, as temperature or humidity of a day may have an effect on Raman fingerprints obtained from the sample. Calibration of the spectrometer was performed using Si wafer as the characteristic Si peak is known, to be located at 520.7 cm^{-1}. After focusing of the microscope, the sample is ready for Raman characterization. Since Raman microscope is an optical microscope, the sample is focused with white light. A 10X optical zoom lens is used in my experiments. Precautions are taken so that the lens tip does not touch the liquid sample's upper surface.

Raman characterization was done with a 532 nm laser excitation wavelength. 325 nm and 785 nm lasers were also attempted, however the 532 nm laser was the most approptiate for Raman spectroscopy of ferritin.

It is very important to note that laser exposure excites the sample, increasing its temperature. Elevated temperatures would lead to evaporation of the liquid with time. To avoid evaporation of liquid samples, I used a short 10 second exposure time, as exposing for too long would evaporate the samples.

NGS LabSpec software was used to display and store the data. A .txt file saved from the NGS LabSpec software contains the obtained Raman spectra information. To analyze the spectra, background subtraction was done by OriginPro 8.5.1 software. Subtraction was performed using a 5^{th} order interpolation.

CHAPTER 4: COMPUTATIONAL METHODS

4.1. The GROMACS Molecular Simulation Package

GROMACS[83–89], which is an abbreviation from GROningen MAchine for Chemical Simulations , is a computational package dedicated to molecular dynamics simulation of biomolecules such as proteins, lipids, and nucleic acids in aqueous environments. GROMACS solves Newton's equations of motions for large systems that may comprise millions of atoms. GROMACS was first designed in 1991 at the Department of Biophysical Chemistry, University of Groningen, Netherlands, in association with Computer Science department of the same university, and has been developed in Groningen University until 2001. Since 2001 it is developed by the GROMACS development team based in KTH Royal Institute of Technology, Stockholm University, and Uppsala University in Sweden.

GROMACS' fast performance is enabled by neighbor search optimization and inner loop performance optimization.[85] The GROMACS package has no built-in force field of its own; however it is compatible with many force fields such as GROMOS-96[90,91] , OPLS-AA[92,93], CHARMM[94] and AMBER.[95] The forces and energies between atoms that GROMACS calculates are of three kinds, bonded interaction, non-bonded interaction and special interaction[85]. Bonded interaction is the interaction between 2, 3 or 4 atoms following harmonic, cubic or Morse potential. Nonbonded interactions are binary inter-atomic interactions, obeying a 6-12 Lennard-Jones potential. Special interactions impose restraints on position, angle or distance of constituents. Position restraints are important for liquid systems. Decreasing position restraints of a macromolecule in

aqueous solution allows the entire system to gradually gain a stable configuration, so that during subsequent computations the macromolecule remains stable in solution.

GROMACS utilizes a "command line interface"- a text-based command input system. The user writes text commands, known as scripts. Also, many files containing topologies and parameters can be used for input and output. Thus, GROMACS is very user friendly. Errors are instantly detected in the GROMACS platform, and help is provided in the help section.[96] GROMACS gives estimated time of arrival (ETA) feedback during the simulation processes, indicating how much time is left to complete the task and when it will be completed. As an output, it generates a trajectory file containing positions and velocities of atoms in the course of the simulations. Conventional simulation conditions involve a rectangular simulation box with periodic boundary conditions, although GROMACS also supports triclinic boxes with periodic boundary conditions.

GROMACS is an open-source software package, published and distributed with source codes and documentations under the GNU General Public License[85]. GROMACS is mostly run in Linux operating systems. However, from GROMACS 4.5 version, the program has been extended to be used in Windows OS platform[87].

In my work, I used GROMACS 5.1.1 on a Linux cluster equipped with 24 quad-core - Intel Xeon E5462 CPUs with 2.80 GHz clock-speed, and total RAM of 384 GB. Along with this, part of my work was done in STAMPEDE2 supercomputer cluster on Texas Advanced Computing Center (TACC), using GROMACS 5.1.2. STAMPEDE2 is also a Linux based cluster with Intel Xeon E5-2680 v4 CPUs with 2.40GHz clock speed,

and each node having 68 cores. The memory of each node is 96 GB DDR RAM and 16 GB high speed Multi-Channel DRAM, or MCDRAM.

4.2. Preparation Of Model For Simulation

The goal of my MD simulations is to understand how iron ions enter into the ferritin globular cage and how the iron ions exit from that cage; a long-sought question that still puzzles the scientific community.

The initial coordinates of atoms in ferritin were obtained from Protein Data Bank, PDB ID 5CZU.[63] After downloading PDB file 5CZU, the file was analyzed. It contained some hetero atoms (HETATM) which were removed for setting up my system. Corresponding CONNECT entries were removed as well. This pdb file has a resolution of 1.6 Å and no atoms or residues were missing, making it an ideal structure to start the simulation. PDB ID 5CZU is a modified ferritin molecule.[63] Residue alanine (Ala119) was replaced with cysteine. Newly incorporated Cys119 is located close to the C3 symmetric channel of ferritin, and contains Sulphur, which can bind gold surface. Although binding of modified ferritin to gold is not explored in this work, this capability is important for future applications. Another cysteine (Cys126) was replaced with alanine to exclude a possibility of conjugation with a ligand[63]. The structure was visually inspected by using visualization software PyMOL[64] and VMD[56].

PDB ID 5CZU, as downloaded from the database, contains coordinates of one subunit. Using PyMOL[64], I generated the 3-fold trimeric structure using a symexp command (Figure 4.1). The command generates neighboring units by utilizing the symmetry information embedded in the pdb file. This way, from the monomer of ferritin, one can generate 3-fold trimer, 4-fold tetramer, and even the whole 24-meric globule.

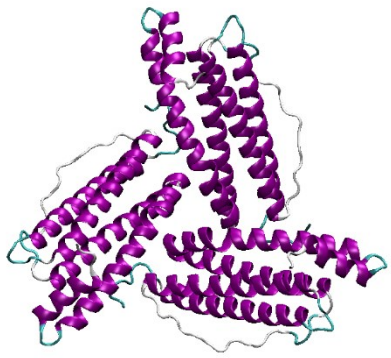

Figure 4.1: PyMOL generated 3-fold ferritin structure.

One important input file for GROMACS operation is the topology file. The default name of topology file is topol.top. Topology file contains force field information required to describe a molecule in the simulation system. At the very beginning, it calls parameters from the force field that is selected. In my work, I chose an OPLS-AA force field for the protein[92,93] and an SPC explicit water model[97]. A script for protein's force field is written as follows:

#include "oplsaa.ff/forcefield.itp".

The script calls parameters from the OPLS-AA force field. Then, the topology defines the protein structure with chains. In my case, since there are 3 chains, itp files are included that contain additional information on position restraints. Position restraints let heavy atoms remain in a fixed position during minimization and equilibration, unless the force acting on them exceeds a specified level.

For solvent, a GROMACS' spc216.gro model is used in this work. This is a three point water model. The script for water topology in topology filereads as follows:

#include "oplsaa.ff/spc.itp".

For iron ions, no forcefield is available in GROMACS. I have determined a non-bonded force field for iron ions based on recently published, extensively optimized Lennard-Jones parameters[98]. A GROMACS-format van der Waals radius of 0.24127 nm and well depth of .039861 $kJmol^{-1}$ were derived from these data[19].

In my simulation work, a 11.24 nm cubic solvation box with periodic boundary conditions was used. The pdb file with co-ordinates of ferritin's trimer is transformed into a GROMACS format "gro" by using a "gmx pdb2gmx" command. The same command also generates the topology file. The unit cell is constructed using a "gmx editconf" command. Solvation included addition of water molecules using the "gmx solvate" command. As the entire system should be charge neutral, I added nine Fe^{2+} ions, to neutralize the -18e charge of my system. Ions were added in PyMOL, by using a "pseudoatom" command.

4.3. Energy Minimization

The purpose of energy minimization is to relax the protein structure. Before adding any water in the solvation box, in-vacuo energy minimization was performed with position restraints to avoid distortion of protein structure. The force constant for each non- hydrogen atom in protein molecule was equal to 100000 $kJmol^{-1}nm^{-2}$ during in-vacuo minimization, which is a very strong position restraints required to keep the protein stable in vacuum. The minimization had a converging limit of 10 $kJmol^{-1}nm^{-1}$ maximum force.

After the water molecules and ions were added, energy minimization of the solvated system was done with six gradually decreasing position restraints on non-

hydrogen atoms of ferritin. Position restraints involved a force constant value decrement of 10 times in each successive step except for the last one, where no restraints were applied. The force constants were equal to 100000, 10000, 1000, 100, 10 and 0 $kJmol^{-1}nm^{-2}$ in the respective six steps of minimization. Starting with a strong position restraint on protein atoms, the minimization proceeded with gradually weakening position restraints. Each minimization involved a maximum number of 3000 steepest descent steps. Minimization may converge before reaching the maximum number of steps, and in my case, this happened in later steps. The steepest descent step size was 0.01 nm, up to allowing a maximum force of 10 $kJmol^{-1}nm^{-1}$.

Energy minimizations were executed by first using "gmx grompp" command with a minimization parameter .mdp file. The command "gmx grompp" assembles the protein structure, topology of the system and all simulation parameters into a binary input file called tpr file. Then the minimizations are done in GROMACS MD engine, executing with "gmx mdrun" command. The command "gmx mdrun" initiates GROMACS MD engine to run the molecular dynamics. Using the flag "-v" in the script is an optional flag, used to show when the simulation will end and show progression of steps as well, the ETA feedback capability of Gromacs I mentioned earlier. The "&" symbol at the end of the script is used to run the process in background. So that I can log off from the server but still the simulation will continue.

After the energy minimization process, a .gro file containing minimized structure is generated.

4.4. Equilibration

After energy minimization is completed, the system is ready for equilibration. Energy minimization provided an initial relaxation of the protein structure. Now, it is important to equilibrate water molecules and iron ions added in the system. Equilibration ensures stability of the system during subsequent production molecular dynamics simulations. In the course of equilibration, temperature is gradually increased in the system up to the level of 310K, at which production MD will be done. Pressure will be also maintained at 1 bar.

I applied the NVT ensemble (number of particles, volume, and temperature constant) using a thermostat with velocity rescaling[99]. Initial velocities of atoms in the system were set at random using a procedure called seed generation. Varying seed generation results in simulations with similar initial positions, but different initial velocities of atoms. In my work, three trajectories with different seed generation were generated for each model. During the first NVT equilibration step, temperature was raised to 310K. After the initial NVT step, I used six successive NVT equilibration steps with decreasing position restraints on non-hydrogen atoms of the protein. Similarly, as for energy minimization. The force constants in each step were similar as for energy minimization: 100000, 10000, 1000, 100, 10 and 0 $kJmol^{-1}nm^{-2}$. The temperature coupling time for each NVT equilibration was equal to 0.01 ps. The number of MD steps for the first NVT equilibration was 50000, i.e. 100 ps; and each subsequent NVT equilibration comprised 25000 MD steps, i.e. 50 ps each; making the entire NVT equilibration process 400 ps long.

Next, NPT ensemble (number of particles, pressure, and temperature constant) was used for equilibration at 1 bar with Parinello-Rahman barostat[100,101], also using velocity rescaling to maintain temperature at 310 K. 50000 integration steps were performed, totaling 100 ps of NPT equilibration. The temperature and pressure coupling time in NPT equilibration were equal to 0.1 pseach. The compressibility was equal to 0.000045 bar^{-1}.

To do NVT and NPT equilibration, a "gmx grompp" command was used to generate a binary edr file. Then "gmx mdrun" command started the GROMACS MD engine for equilibration. During NPT equilibration, while using a "gmx grompp" command, an additional "-t" flag was used to load velocities generated during previous NVT steps, and other parameters. The resulting structure was ready for production MD simulations.

The entire process flow chart of the MD simulation is summarized in Figure 4.2.

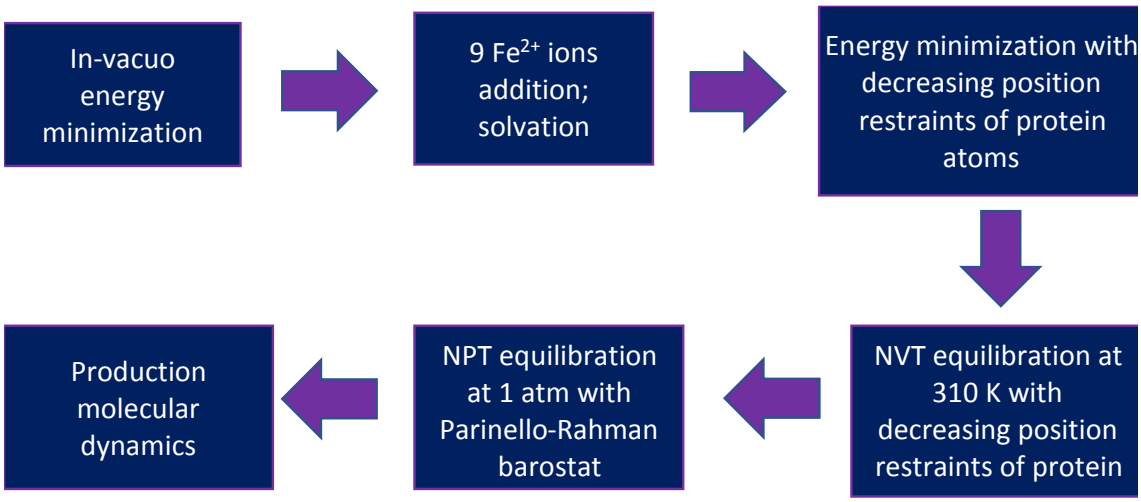

Figure 4.2: Process flow chart of molecular dynamics simulation.

4.5. Production MD Simulations

After successful equilibration, molecular dynamics simulations were performed to generate time series of all atoms' positions and velocities, known as MD trajectories. The GROMACS MD engine was used. The protocol was similar to the equilibration steps, involving "gmx grompp" and "gmx mdrun" commands. The output (checkpoint) file generated after NPT equilibration was loaded as an input using a "-t" flag.

An integration time-step of 2 fs was used for all MD simulations. For neighbor searching in MD process, a Verlet cutoff-scheme was employed. An 1.4 nm cutoff radius was used for van der Waals and short-range electrostatic interactions. Long range electrostatic interactions were accounted for with a particle-mesh Ewald (PME) summation using a 4^{th}-order interpolation and a maximum grid dimension of 0.135 nm. The neighbor list was updated after every 10 integration time-steps, or 20 fs. The LINCS algorithm[102] with 4^{th} order expansion and 2 iterations was used to constrain bond lengths for the protein. Water molecules were constrained with the SETTLE algorithm[103].

In my production MD simulations, a physiologically relevant temperature of 310 K was maintained using a velocity rescaling thermostat with a stochastic term[99] ensuring a proper canonical ensemble. Protein and non-protein groups were coupled separately to respective temperature baths. Pressure of 1 atm was maintained with a Parrinello-Rahman barostat[100,101]. Other details of maintaining temperature and pressure can be found in Section 4.4.

Production MD was performed long enough to obtain a desired duration of MD trajectories. Continuation of interrupted simulation is possible by loading output data from previous production MD runs.

Output generated after production MD simulations includes a binary full precision trajectory file containing time dependent coordinates and velocities of each atom. Visualization software such as VMD reads this file, displays graphical animation of the process, and provides analysis of the results.

4.6. Visualization And Analysis Softwares

Data files that are used in GROMACS for input or output are either ASCII or binary, and they contain coordinates and velocities information. Analyzing this information reveals the nature of chemical or physical processes represented by the simulation. Initial step in this analysis is to visually inspect the process under investigation. Table 4.1 lists visualization software that was extensively used in my work, and specific functions that I used. A lot of analyses beyond simple visualization can be done in each software. Note that sometimes, one software is better suited than other to perform a certain task.

Using VMD 1.9.2, I rendered the trajectory animation as a movie by using VMD movie maker extension tool. VMD is also extensively used in my work for post simulation analyses. Using snapshot rendering mode with trajectory loading settings, I used VMD to take screenshots of each timesteps and then by using VideoMach software, those screenshots were compiled together to create the movie. Also, by using VMD, I visually represented the protein in many user controlled ways- varying atom rendering options in different ways and by applying different colors in each atom-type or residue-type or any other subset of similar atoms. I utilized VMD's graphical interface for performing structural analysis. Also, VMD's text interface enabled by Tcl embeddable

parser were extensively used. This interface allows inputting script commands for complex functions, such as selecting atoms up to certain distance form a reference point, removing particular molecules or residues, measuring distance between two atoms, zooming in the chemical structure with same magnification, etc. It was used to specifically show secondary structures, side chains, solvent accessible surface area (SASA), electrostatic potential on the surface, diffusion path of an ion or atom, etc. It should be noted that, merely visualizing protein in different ways is only a small part of vast analyses possible to do in VMD. For example, radial pair distribution function and RMSD trajectory tool were also used in my work to generate RDF and RMSD plots of water molecules and iron ions respectively. RDF is enabled by an extension tool, measuring distribution of one atom type with respect to another atom type. I measured g(r), the radial pair distribution function of oxygen atom of water molecules with respect to iron ion that enters into the channel. The result of my RDF analysis of water solvation shell is briefly discussed in chapter 5. This RDF plot is generated over a time frame, which can be specified in VMD command prompt. I also used RMSD trajectory tool to generate RMSD plot of iron ions. The tool is capable of skipping time frames, thus accommodating large trajectories with many MD steps, for example in my case around 24 ns of simulation trajectories. "All to all" RMSD is possible, i.e. all molecules against all molecules or all frames against all frames. I did RMSD of iron ion that enters the channel, with respect to its first frame against all frames. Multiplot VMD plugin composes the coordinate data file, accessible as .txt format for MS Excel. No selection modifiers were used in my analysis as the analysis is limited to one ion at a time.[104,105]

The STRIDE algorithm[106] as implemented in VMD was used to identify protein's secondary structures.

Table 4.1: Visualization and analysis software for MD analysis

Name of software	Functions usable in protein simulation
PyMOL	Visually observing pdb file and gro file as 3D, ion addition, doing symmetry operations to form multimers, rendering images.
VMD (Visual Molecular Dynamics)	Observing pdb file and gro file in 3D, RMSD plot generation, RDF plot generation, rendering solvent accessible surface area (SASA) of protein, trajectory animation view, electrostatic potential coloring, rendering images and movies.
PV (Protein Viewer)	JavaScript viewer to visualize 3D proteins in web browsers, rendering images.
JMOL	HTML5 viewer to visualize 3D chemical species
Adaptive Poisson-Boltzmann Solver (APBS) in the PDB2PQR server	To illustrate electrostatic potential on protein structure.

CHAPTER 5: COMPUTATIONAL RESULTS

5.1. Transport Of Fe Ions Through Ferritin's Channel

The ferritin monomer of PDB ID 5CZU was used to construct the 3-fold structure expressing the channel responsible for transport of iron ions, as described in Sect. 4.2. The trimer structure contains only atoms of the protein. Some atoms belong to main chain of the protein, and others to side chains.

After solvation, 9 Fe^{2+} ions were added in the solvation box. In one setup, ions were added outside the hypothetical ferritin globule, i.e. on the convex side of the 3-fold channel, as shown in Figure 5.1(A, B). The approximate distance of Fe^{2+} ions from the channel was 0.5-1.1 nm. In another setup, I added Fe^{2+} ions on the concave side of the channel, mimicking ions added inside the hypothetical ferritin globule. In the course of NPT and NVT equilibrations the ions have moved, still remaining in close vicinity of the channel (Figure 5.2).

As I applied three different sets of initial velocities of atoms with the same initial positions, three statistically independent MD trajectories were produced for each structure. I denote the three trajectories for ions added outside of the trimer by OA, OB, and OC. Similarly, three trajectories for ions added inside are denoted by IA, IB, and IC. Table 5.1 lists the six trajectories obtained. At least 20 ns of simulations were completed for each of the trajectories. I found similar result for all three sets in most cases. Unless otherwise mentioned, I are displaying results of OA and IA trajectories as a representative outcome of my simulations.

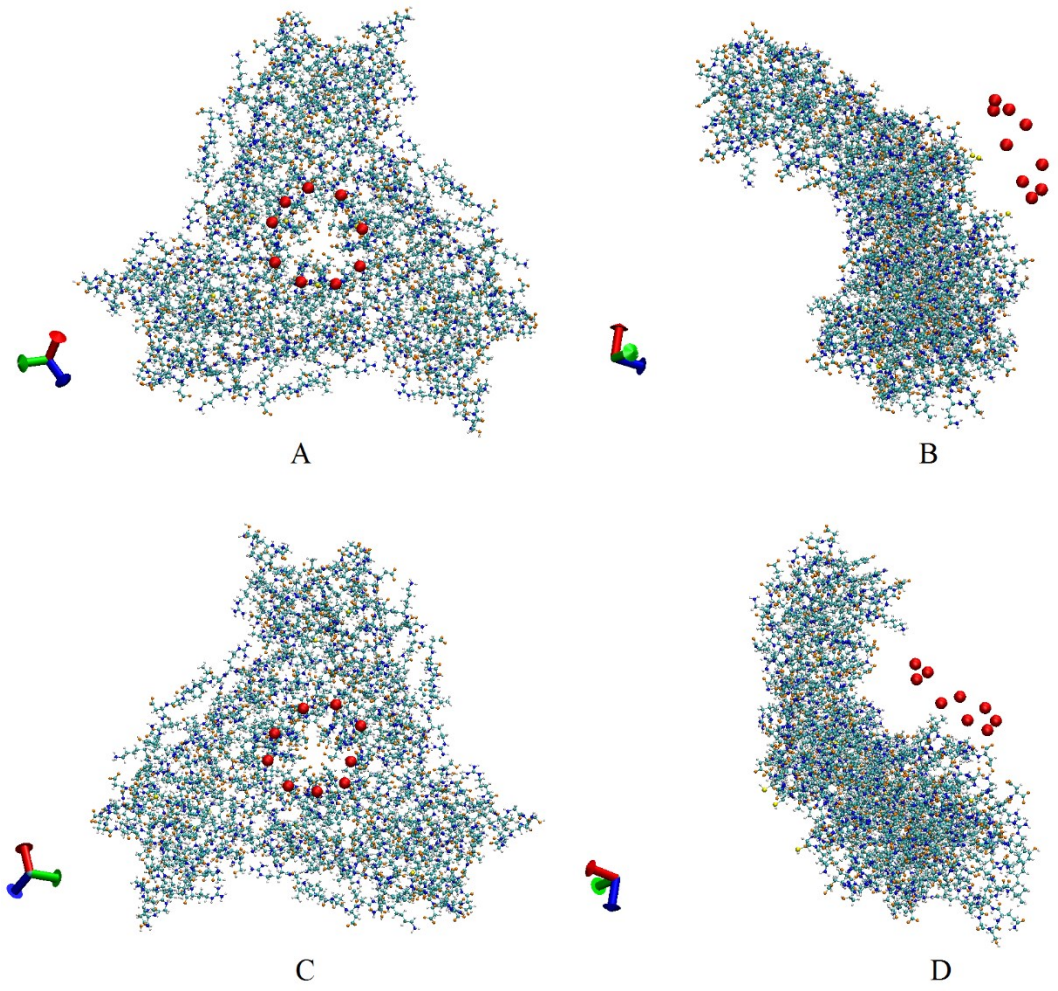

Figure 5.1: Initial structures of ferritin's trimer with nine iron ions before equilibration: A) Fe^{2+} ions added outside of the ferritin trimer, B) side view of ions outside the trimer, C) Fe^{2+} ions added inside of the ferritin trimer, D) side view of ions inside the trimer. Iron ions are shown with red spheres.

Figure 5.3 shows snapshots from production MD trajectory OA. It can be seen that at 1.4 ns, one of the ions almost entered the channel, and a second ion approached it. During subsequent simulations, the first ion remained in the channel, and the second one continued approaching it. The second ion entered the channel after approximately 1.5 ns from the beginning of production simulations.

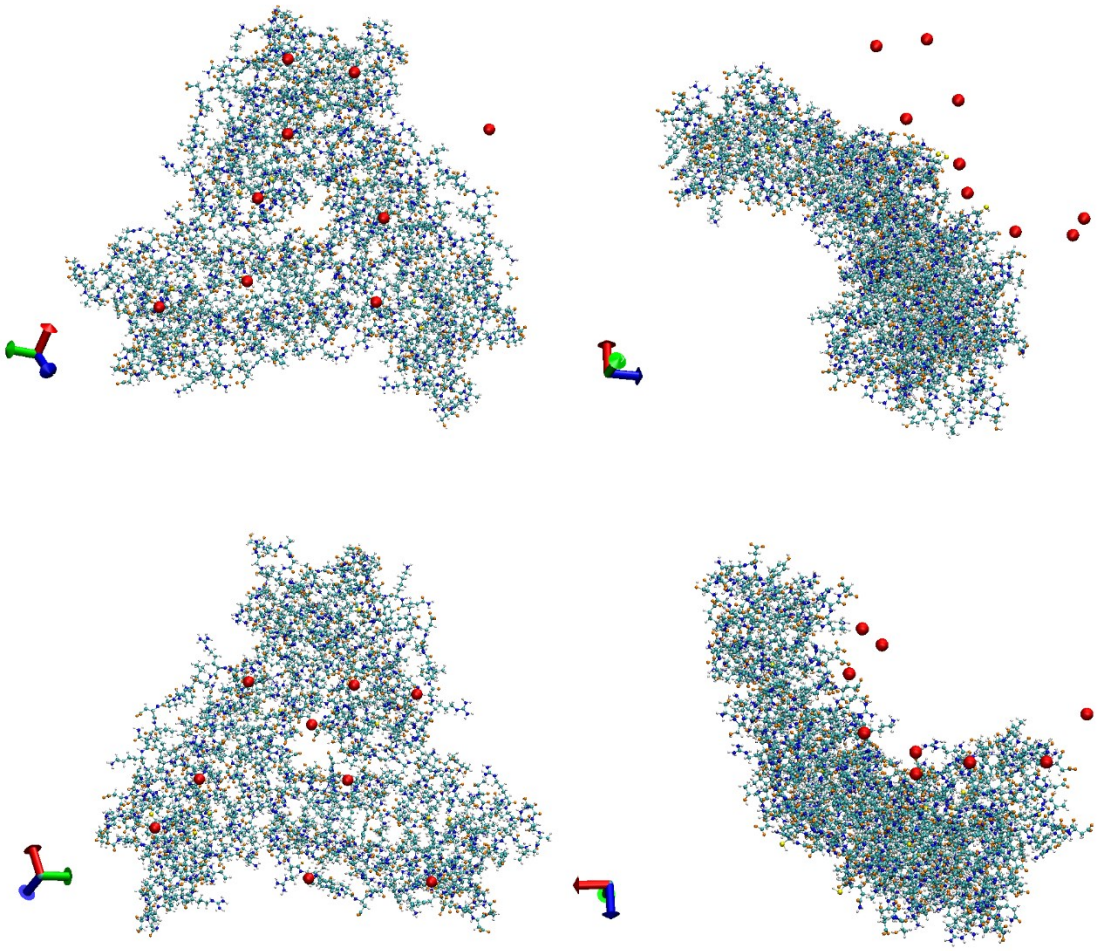

Figure 5.2: Iron ion positions after equilibration: A) ions added outside of the trimer, B) ions added outside side view, C) ions added inside of the trimer, D) ions added inside side view. Ions are shown by red spheres.

As the second ion moves into the channel, it repeals the first ion inside the channel. At approximately 11.8 ns, the first ion completely exited from the channel, expelled by the second ion. Simulation up to 20 ns shows a complete expulsion of the first ion. A similar trend was observed in two other trajectories OB and OC, with ions

entering the channel in less than 2 ns. In trajectory OC the first ion did not yet fully exit by 20 ns, however it was in the process of ejection from the channel. In trajectory OB the first ion completely exited from the channel by approximately 8.8 ns, expelled by the second ion; and the third ion entered the channel at 4.2 ns. By 20 ns both the second and the third ion remained inside the channel, following the path of the first ion.

Table 5.1: Sets of production MD simulations.

Ion position	Production MD simulation set			Simulation time
Ions added outside of the trimer	OA	OB	OC	20 ns
Ions added inside of the trimer	IA	IB	IC	20 ns

Ions added inside of the ferritin trimer showed a similar trend, as one can see in Figure 5.4. In trajectory IA, the first ion entered the channel at around 1.3 ns. However, a second ion did not enter into the channel in any of my simulations with ions added inside of the trimer. In trajectory IA two ions, the second and the third one, are seen in close proximity of the channel at 20 ns, following the first ion that is already in the channel. However, I did not observe entering of the second and third ion in the channel. In simulations IB and IC, only one ion followed the first ion, but the second one did not enter the channel. By 20 ns of the simulation, the first ion remained in the channel, and the second ion was in close proximity of the first ion, yet outside of the channel.

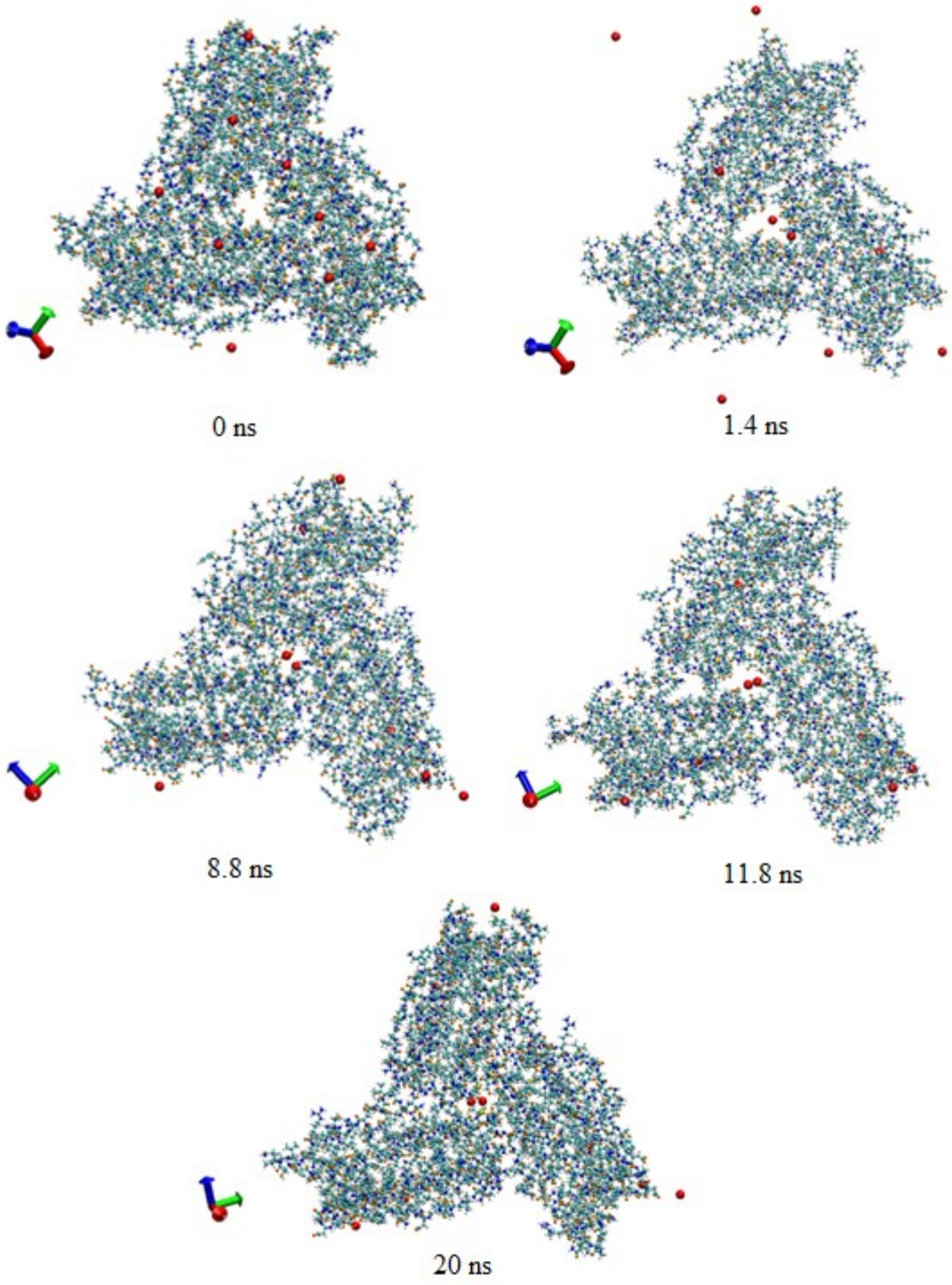

Figure 5.3: Snapshots of the trimer with Fe^{2+} ions added outside at different simulation times.

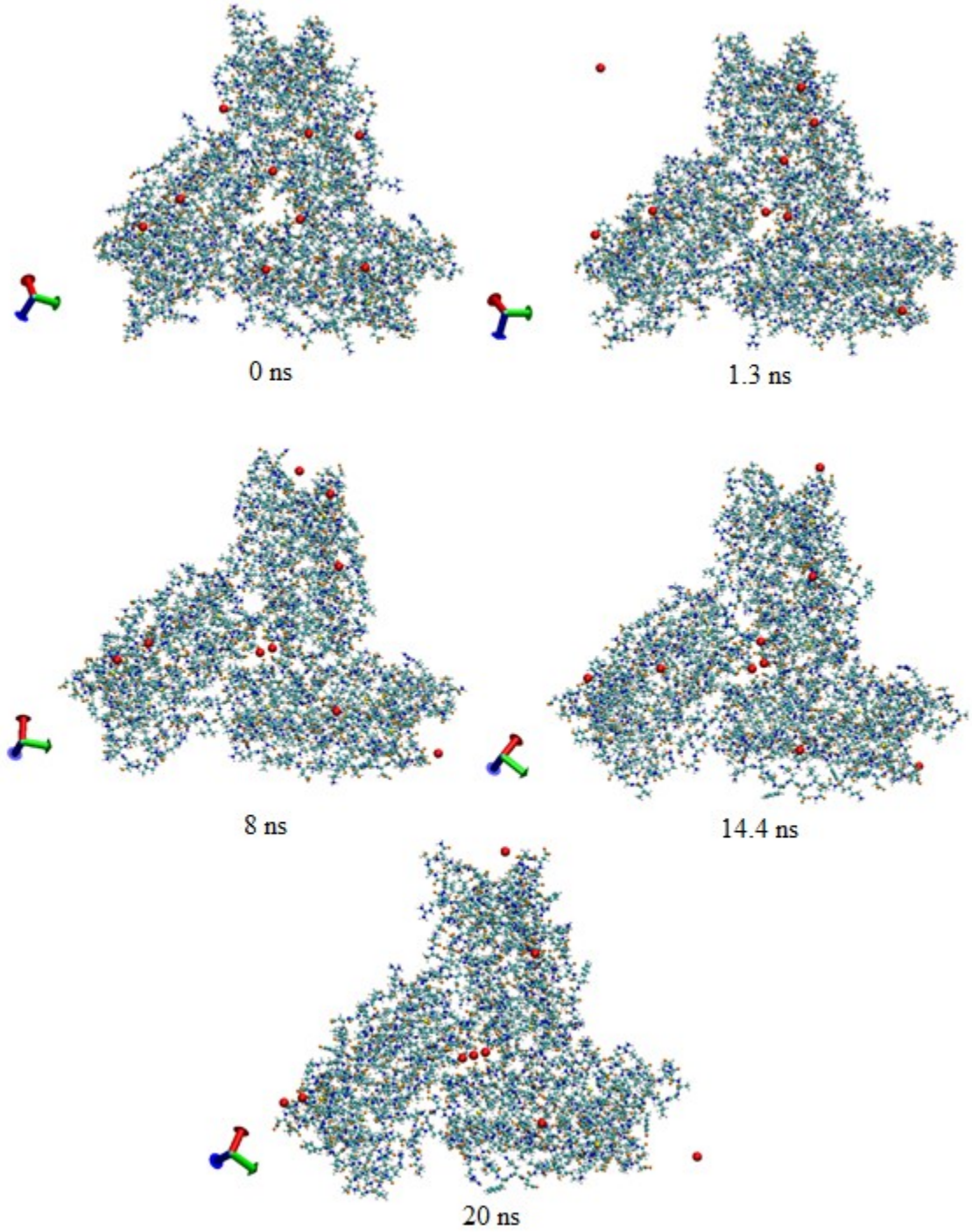

Figure 5.4: Snapshots of the trimer with Fe^{2+} ions added inside. Ions are shown with red spheres.

Analysis of root-mean-square deviation of atomic positions (RMSD) plots of the iron ions as they travel through the channel helps understanding this process better. Figure 5.5 depicts an RMSD plot of the first ion from trajectory OA, computed with respect to initial position of the ion after equilibration. The RMSD plot illustrates how the ion moves during the entire simulation. When after equilibration the ion was approaching the channel, the RMSD plot exhibits a quick increase. When the ion entered into the channel at around 1.4 ns, the plot reaches a plateau. Although random fluctuations due to diffusional nature of ion's motion are visible, the average deviation remains uniform from this point. When the ion exited the channel at 11.8 ns, I can see that the RMSD increases again, due to ion's displacement away from its initial position.

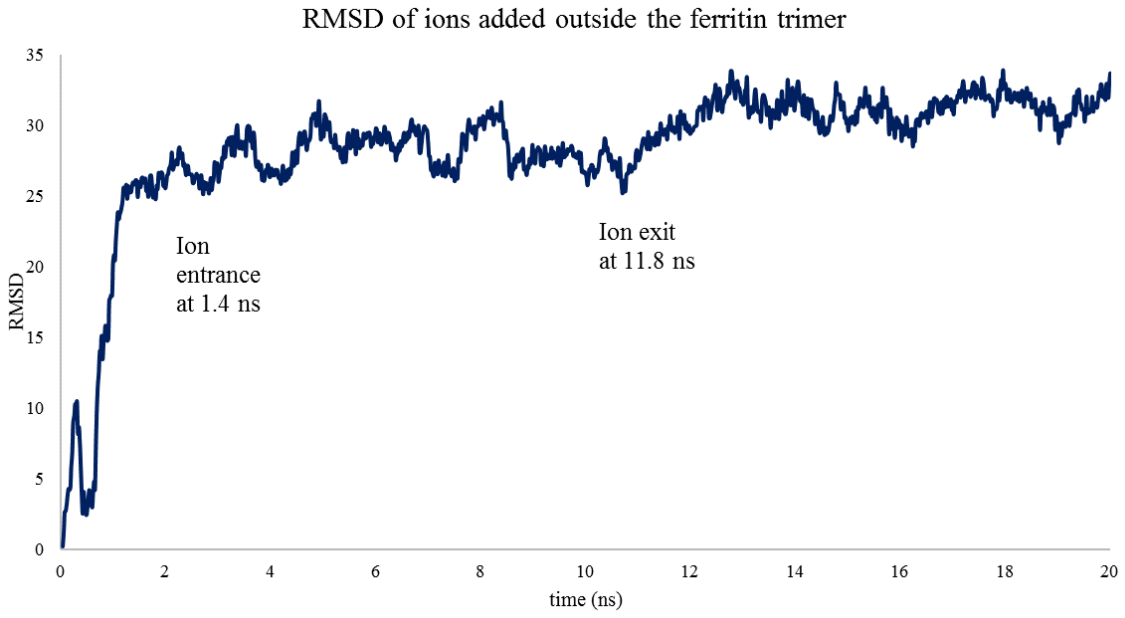

Figure 5.5: RMSD plot of the first ion that entered the channel from outside, as illustrated in figure 5.3.

Figure 5.6 depicts an RMSD plot of ion added inside of the trimer from trajectory IA. The plot shows that the ion approached the channel and entered it at approximately 1.3 ns. While remaining inside the channel, the ion continued moving predominantly forward until approximately 8 ns. Then, after some random walking, the ion started moving back at approximately 12 ns. This reverse motion occurred until ~18 ns, when the ion started moving forward again. Note that the second ion approached the channel at 3 ns, and the third ion approached the channel at 14.4 ns. I hypothesize that the third ion's arrival in the vicinity of the channel ion might cause the return of forward motion.

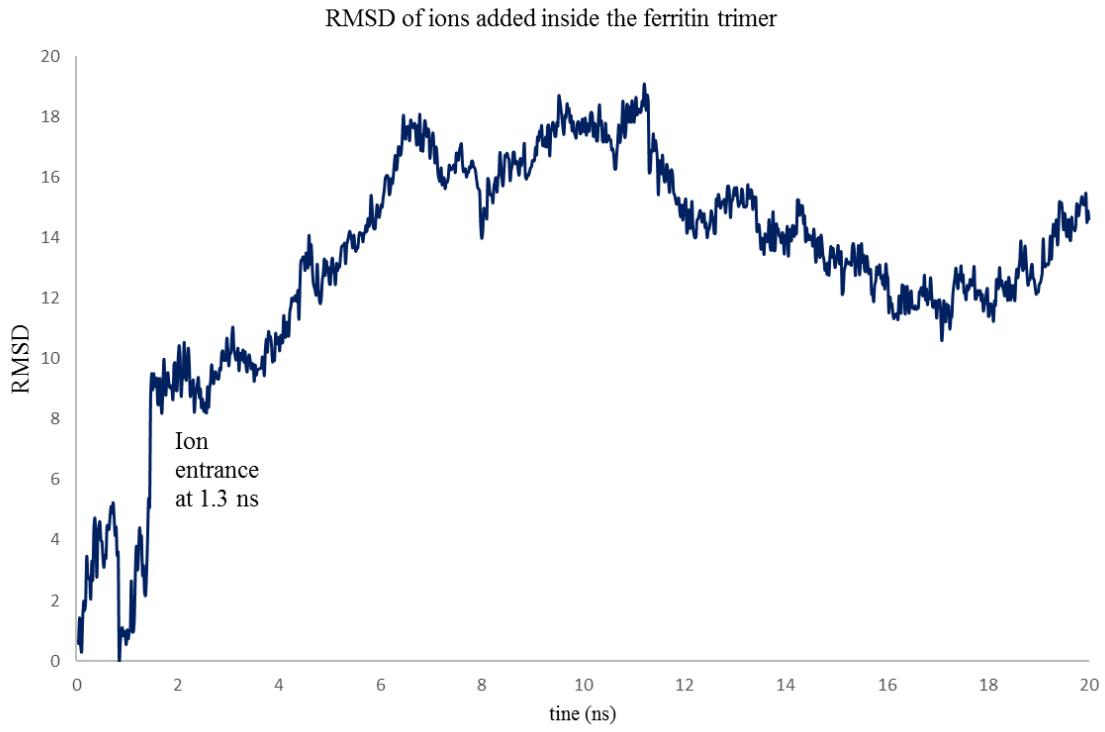

Figure 5.6: RMSD plot of the first ion that entered the channel from inside, as illustrated in figure 5.4.

5.2. Electrostatic Potential Around Ferritin's Channel

As the results in Section 5.1 indicate, iron ions tend to quickly approach ferritin's channel and enter it from either side. To better understand driving forces of this process, electrostatic potential of ferritin was calculated. For this purpose, I used Adaptive Poisson-Boltzmann Solver (APBS) software package in the PDB2PQR server[107]. This software calculates electrostatic properties of molecules using PDB files as the input.

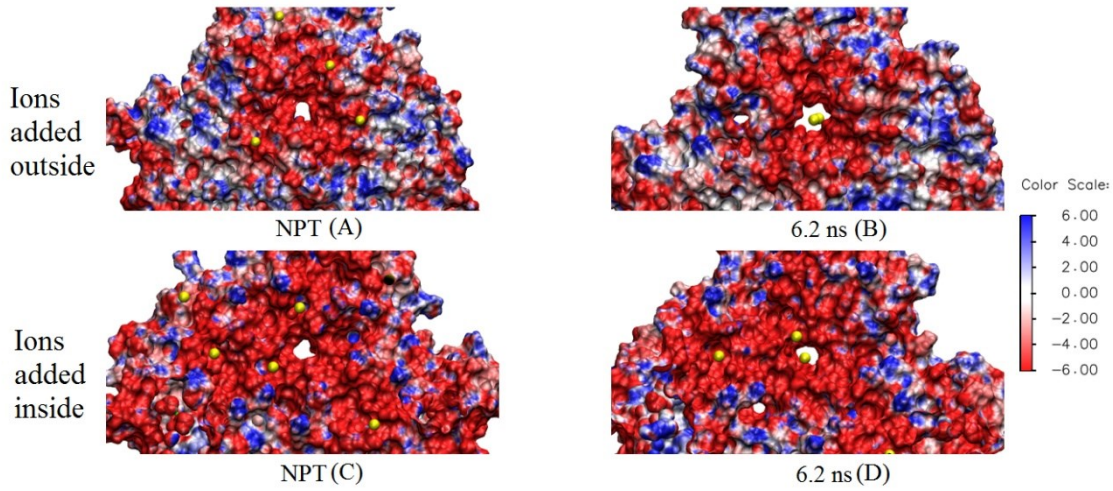

Figure 5.7: Electrostatic potential, color-coded and mapped onto the solvent-accessible surface of ferritin trimer after equilibration (left), and when at least one iron ion entered the channel (right). The ions are shown as yellow spheres. Two panels on the top show outer surface of the trimer, and those on the bottom show inner surface.

Figure 5.7 shows electrostatic potential, color-coded and mapped onto the solvent-accessible surface of ferritin's trimer immediately after equilibration, and later when at least one ion entered the channel. As it can be seen in the color scale of the figure, blue color shows positively charged regions, and red color shows negatively charged regions. The surface of the channel is negatively charged, and the channel is

surrounded by extensive negatively charged regions. The presence of negative charge in the vicinity of the 3-fold channel of ferritin explains the quick entering of iron ions in the channel that I observe. The negative regions attract the iron ions near the channel, eventually driving the ions' entering in it.

5.3. Coordination Of Fe Ions In The Channel

Figures 5.8 and 5.9 show a Fe^{2+} ion in a stable position inside ferritin's channel. The ion is found in close proximity of carboxylate groups from residues Glu130 (Glutamic acid) of the three chains of ferritin, as shown in the figures. This is not surprising, as such groups are negatively charged. However, the ions always remain at a distance from these groups. The reason is clarified by a close-up of iron ion in the channel shown in Figure 5.9. Water molecules, shown by V-shaped "licorice" models, are surrounding the iron ion. This solvation shell results in the iron ion's maintaining of a distance with respect to ferritin's residues.

Visualization of the Solvent Accessible Surface (SAS) of ferritin's channel further supports the above argument. Figure 5.10 (A) depicts SAS in the region of the iron ion inside the channel, and figure 5.10 (B) shows SAS around the ion when it exits from the channel. All throughout, a clear hollow space between iron ions and the channel's SAS is evident.

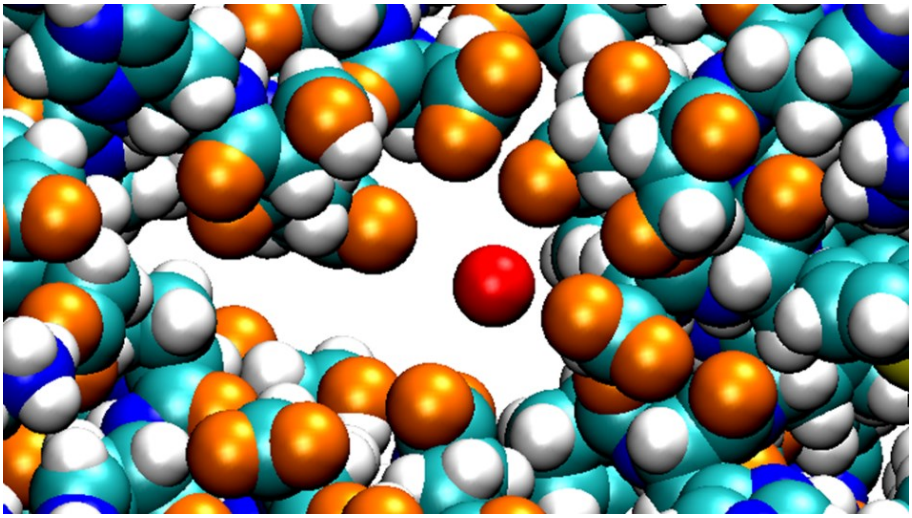

Figure 5.8: Iron ion (red sphere) surrounded by carboxylate group of Glu130 residue in the 3-fold channel of ferritin.

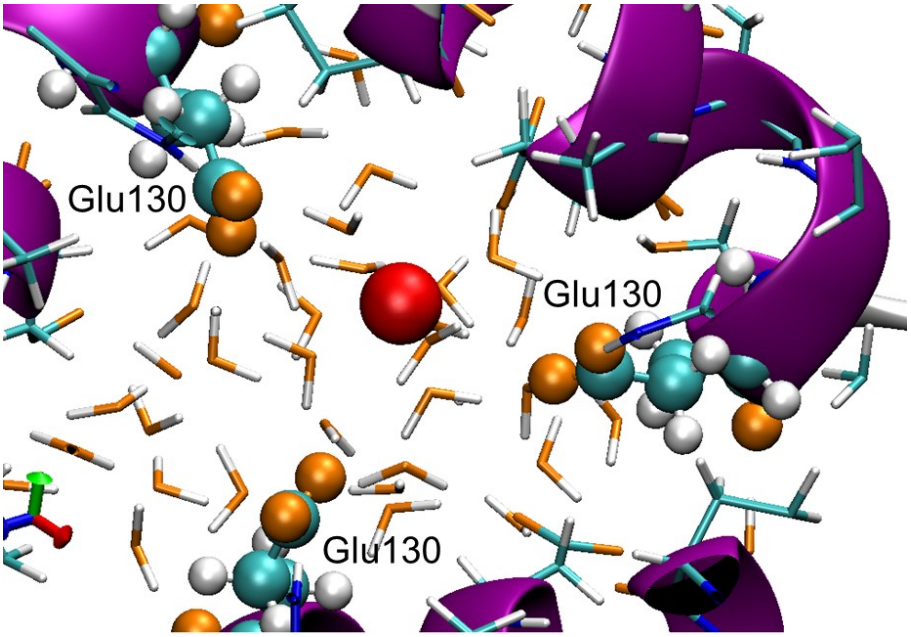

Figure 5.9: Close-up of Glu130 residues of three chains of ferritin and water solvation shell surrounding a Fe^{2+} ion in the channel of ferritin.

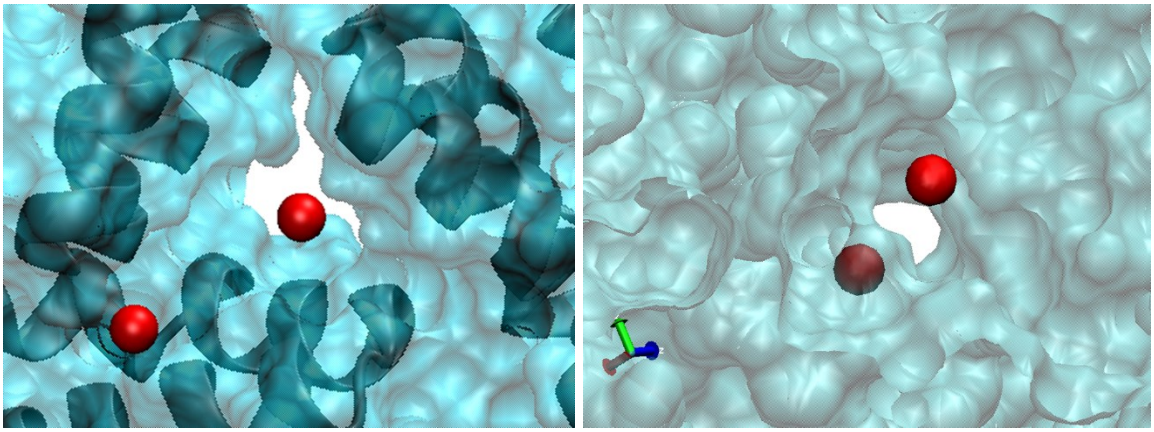

A B

Figure 5.10: Solvent Accessible Surface (SAS) of ferritin's channel with Fe^{2+} ion in the channel at 1.4 ns (A), and the ion exiting the channel while second ion approaching at 11.8 ns of the simulation for ions added outside of the trimer.

Since water molecules surrounding the ion in the solvent-accessible space appear to play an important role in the ion transport through the channel, radial distribution functions (RDF) of water molecules around the ions were calculated. The RDF of water molecules allows quantifying solvation shells around the iron ion. Figure 5.11 shows solvation shells for different iron ion positions, computed with reference to oxygen atoms of water molecules for the trajectory OA of ions added outside.

As shown in Figure 5.11, two solvation shells surround the iron ion. The narrow strong peak at a 0.21 nm distance from the ion is the first solvation shell. This shell remains unchanged all the way throughout the ion's path. The smaller and broader peak with a maximum at 0.43 nm represents the second solvation shell. The second solvation shell experiences slight changes over the ion's trajectory. From 0 to 0.8 ns, when the iron ion approaches the channel, but is still outside of the channel, the average number of water molecules in the second solvation shell is the highest. From 0.8 to 1.6 ns, the ion

entered into the channel. Narrow channel pathway results in slightly lesser average number of water molecules in the second solvation shell. The ion exits the channel between 11 and 11.8 ns, and the RDF plot shows an increased number of water molecules. After 20 ns, I can see more water molecules surrounding the ion.

Figure 5.12 presents an RDF plot of trajectory IA (ions added inside of the trimer), calculated for the iron ion that entered the channel, with reference to oxygen atoms of water molecules. Two solvation shells are clearly visible. The first solvation shell remains unchanged throughout the trajectory, and the second one exhibit slight changes. When the ion enters I channel, I can see more water molecules in second solvation shell. During subsequent simulations, ion remains inside the narrow channel, resulting in a somewhat lesser number of water molecules in second solvation shell.

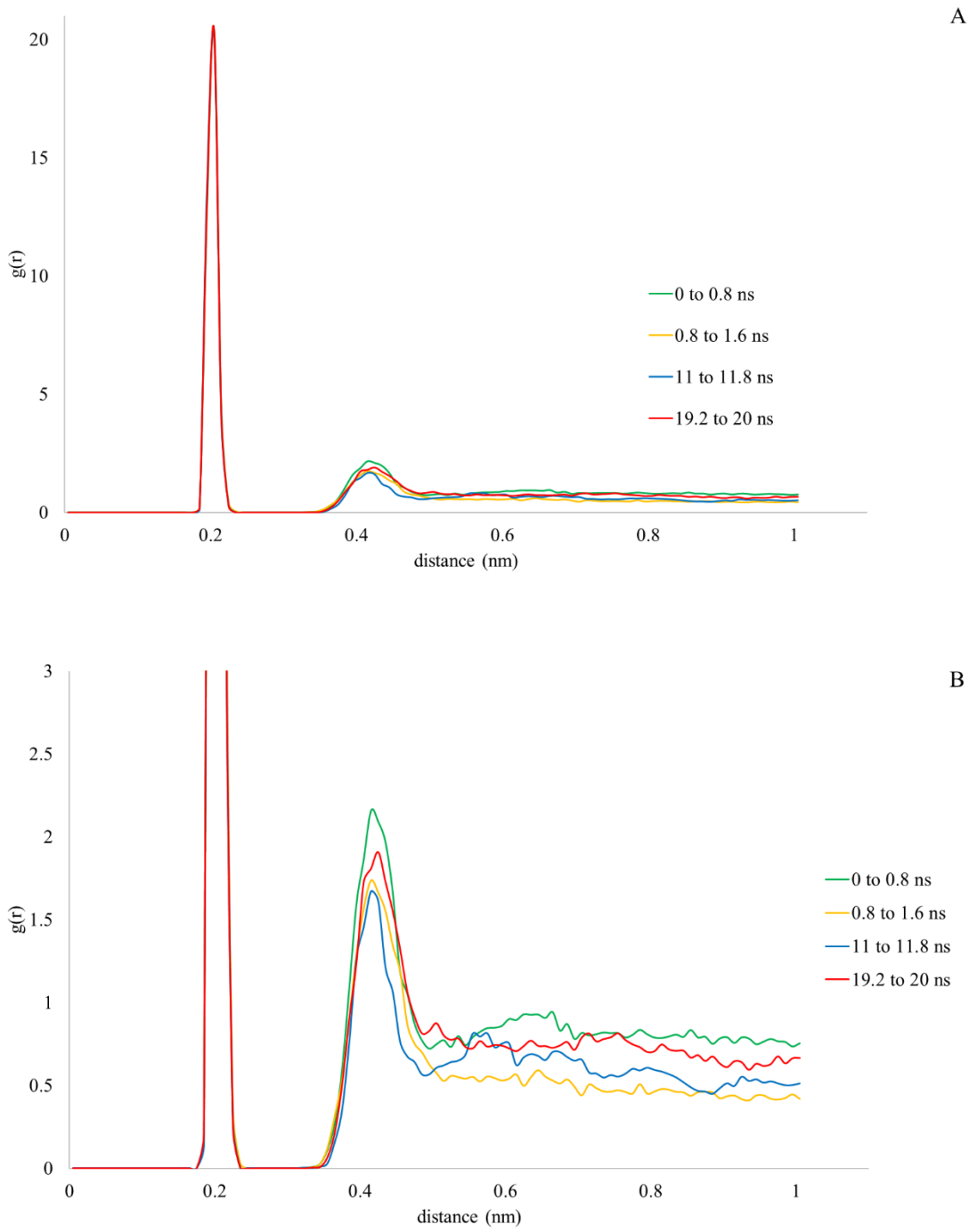

Figure 5.11: RDF of iron ion entering the channel from outside.

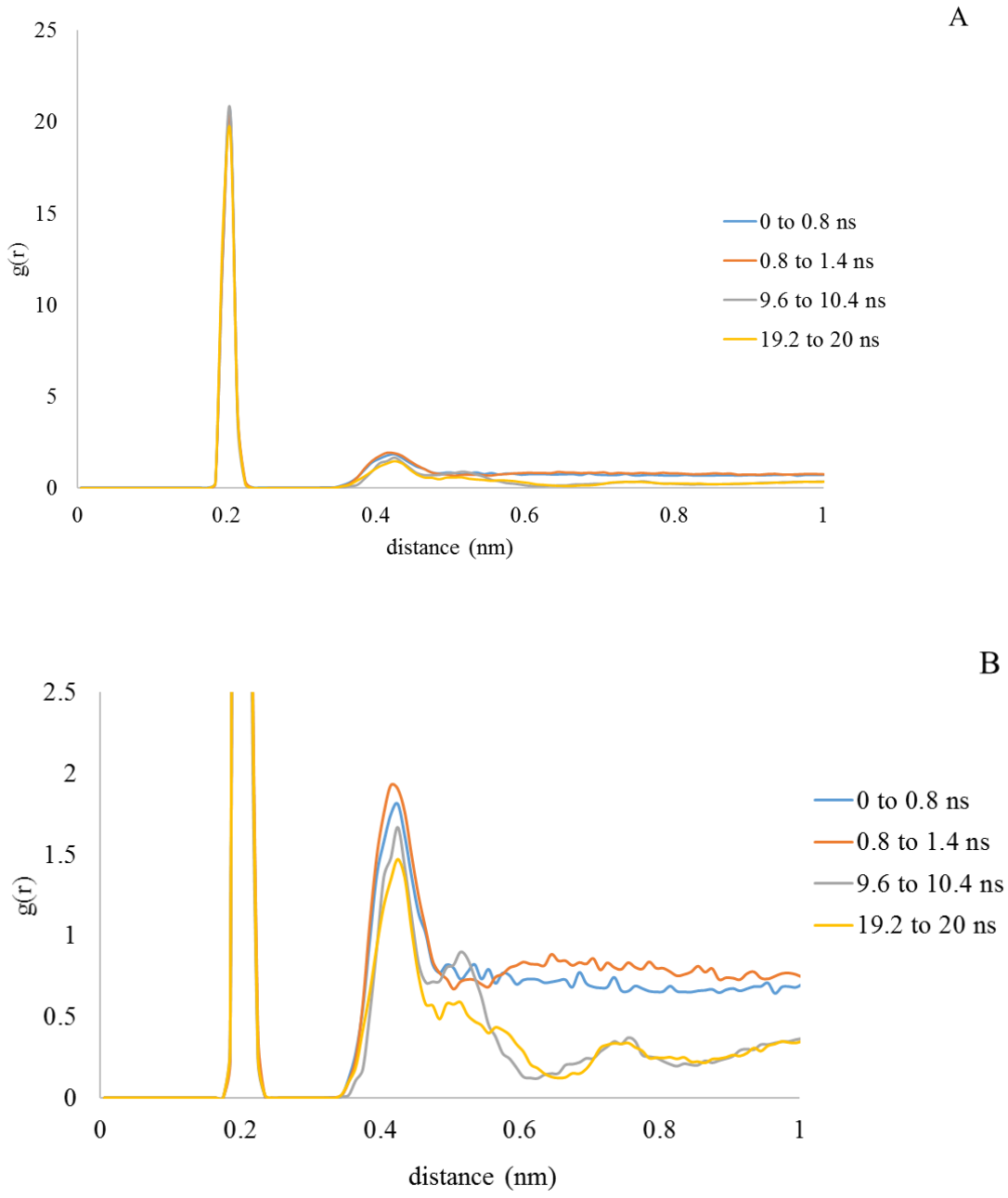

Figure 5.12: RDF of iron ion entering the channel from inside.

CHAPTER 6: EXPERIMENTAL RESULTS

6.1. Raman Spectra Of Ferritin

Raman spectra of ferritin solution were acquired on Si substrates. A baseline subtracted Raman spectrum of ferritin solution is shown in Figure 6.1. The bands of Raman spectra were attributed to various functional groups of ferritin, and also iron compounds. Table 6.1 lists the hypothetical band assignments. These assignments were done based on published literature[16,108–116].

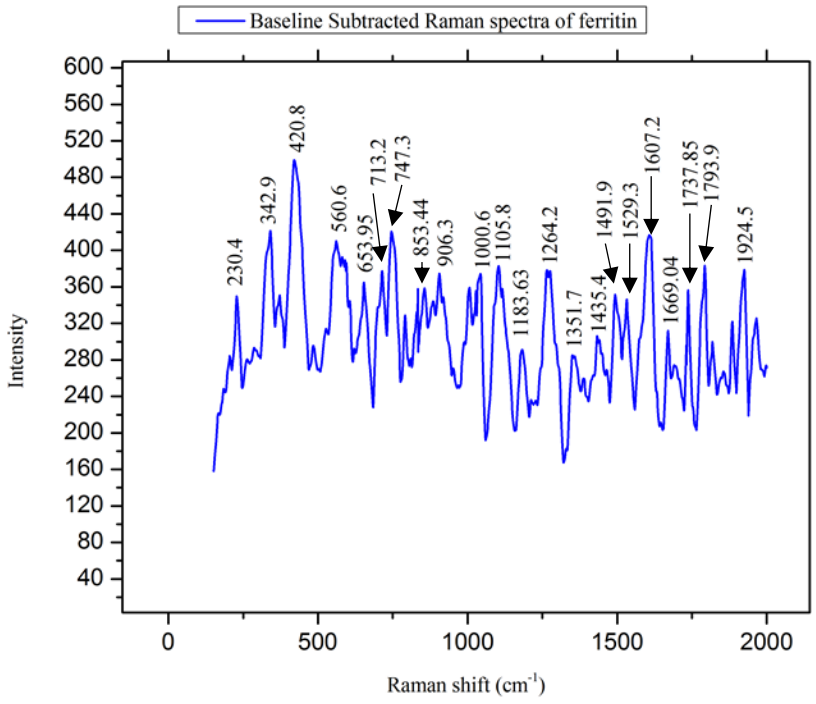

Figure 6.1: Baseline subtracted Raman spectrum of ferritin on Si substrate.

Table 6.1: Hypothetical Raman band assignments of ferritin solution (from Refs. 16, 108-116)

Raman shift (cm^{-1})	Band assignment
230.4, 342.9, 420.8	Iron compounds
560.6	Phe, Tyr
653.95	Tyr
713.2	CH_2
747.3	Trp ring
787.8	CH_2 rocking
853.44, 906.3	C-C, C-O-C, Tyr, Trp
1000.6	Phe
1043.34	C-C, Phe ring bend
1105.8	C-N, C-O
1264.2	Asp, Glu
1351.7	Trp
1435.4	CH_2 deformation; CH, CH_2, CH_3 bending
1491.9	Phe, C-C ring
1529.3	Double bonds of C=C, C=N, C=O
1607.2	Phe, aromatic rings
1669.04	Amide I, C-O, C=C
1737.85	Asp
1880- 1970	C=C, C=N, C=O

(Tyr, $C_9H_9NO_2$). Additionally, Phe has four more band assignments in the spectrum at 1000.6 cm^{-1}, 1043.34 cm^{-1}, 1491.9 cm^{-1}, and 1607.2 cm^{-1}; specifically, 1043.34 cm^{-1} is expected to originate from Phe's benzene ring bending. Tyr has three more bands observed in the spectra- 653.95 cm^{-1}, 853.44 cm^{-1}, and 906.3 cm^{-1}.

Tryptophan (Trp, $C_{11}H_{10}N_2O$), has characteristic peaks at 747.3 cm^{-1}, 853.44 cm^{-1}, 906.3 cm^{-1}, and 1351.7 cm^{-1}, where the band at 747.3 cm^{-1} is assigned to Trp ring. Aspartic acid (Asp, $C_4H_5NO_3$) and Glutamic acid (Glu, $C_5H_7NO_3$) both have Raman bands at 1264.2 cm^{-1}. Additionally, Asp has another Raman band at 1737.85 cm^{-1}. Other Raman peaks, as indicated in the table, are expected to originate from C, N, and O bonds.

The low-shift bands at 230.4 cm^{-1}, 342.9 cm^{-1}, and 420.8 cm^{-1} have been hypothetically attributed to vibrations of Fe–O coordination bonds of iron ions present in ferritin.

Interestingly, Raman spectra of powdered apo-ferritin without ferrihydrite mineral on a Si substrate shows similar bands, with some occasional peak shifts or intensity variations. For example, the peak at 853.44 cm^{-1}, representing C-C, C-O-C, residue Tyr, and residue Trp, is not present in powdered apo-ferritin. I can see only a very small peak in that region, whereas in ferritin solution, this peak is well pronounced. Similarly, Raman band at 1529.3 cm^{-1} representing vibrations of double bonds is very weak in powdered apo-ferritin. The Raman band at 1264.2 cm^{-1} that I attribute to Phe and Glu in ferritin solution has shifted to 1275.2 cm^{-1} in powdered ferritin. For residue Phe and vibrations of aromatic rings, I can also see a shift from 1607.2 cm^{-1} in ferritin solution to 1614.1 cm^{-1} in powdered apo-ferritin.

Instead of the three low-shift peaks at 230.4 cm^{-1}, 342.9 cm^{-1}, and 420.8 cm^{-1} that have been attributed to iron compounds, in apo-ferritin, I observe three peaks at slightly different positions, 228.6 cm^{-1}, 341.4 cm^{-1}, and 424.8 cm^{-1}. A possible interpretation is that the lyophilized powdered ferritin sample still contain some iron ions.

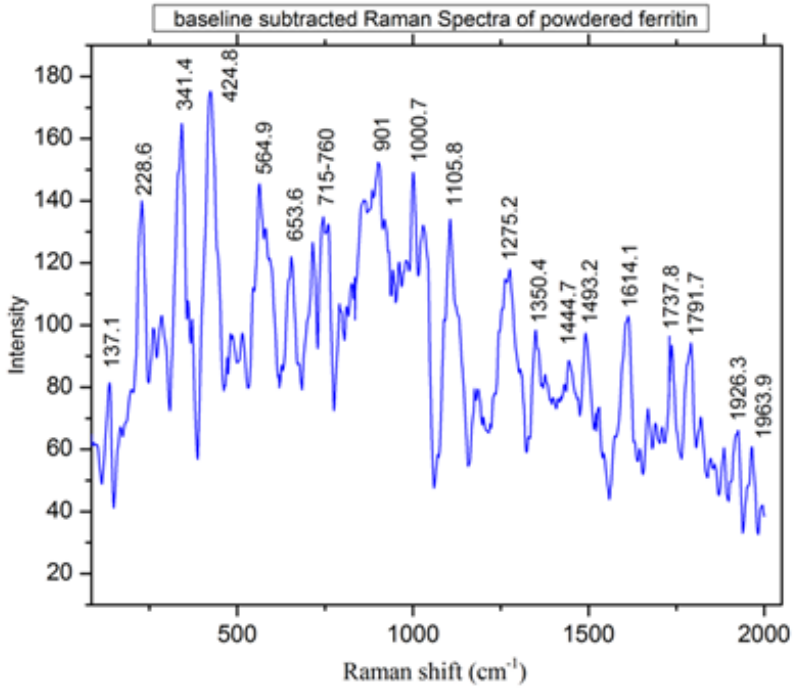

Figure 6.2: Raman spectrum of powder apo-ferritin on Si substrate.

In the next experiment, a drop of DI water was deposited on powdered apo-ferritin on a Si slide, and the sample was incubated for approximately 18 hours in a humid environment in two-compartment Petri dish at room temperature. This prevented evaporation of water during the incubation, and powdered ferritin remained in water. Raman spectra were obtained in two ways. Initially no filter were applied, which corresponded to a 50 mJ laser energy on the sample (Figure 6.3). During this experiment, the water evaporated due to laser exposure. In another experiment, a filter with 50% reduction of excitation power was applied, and the water remained on the slide (Figure 6.4).

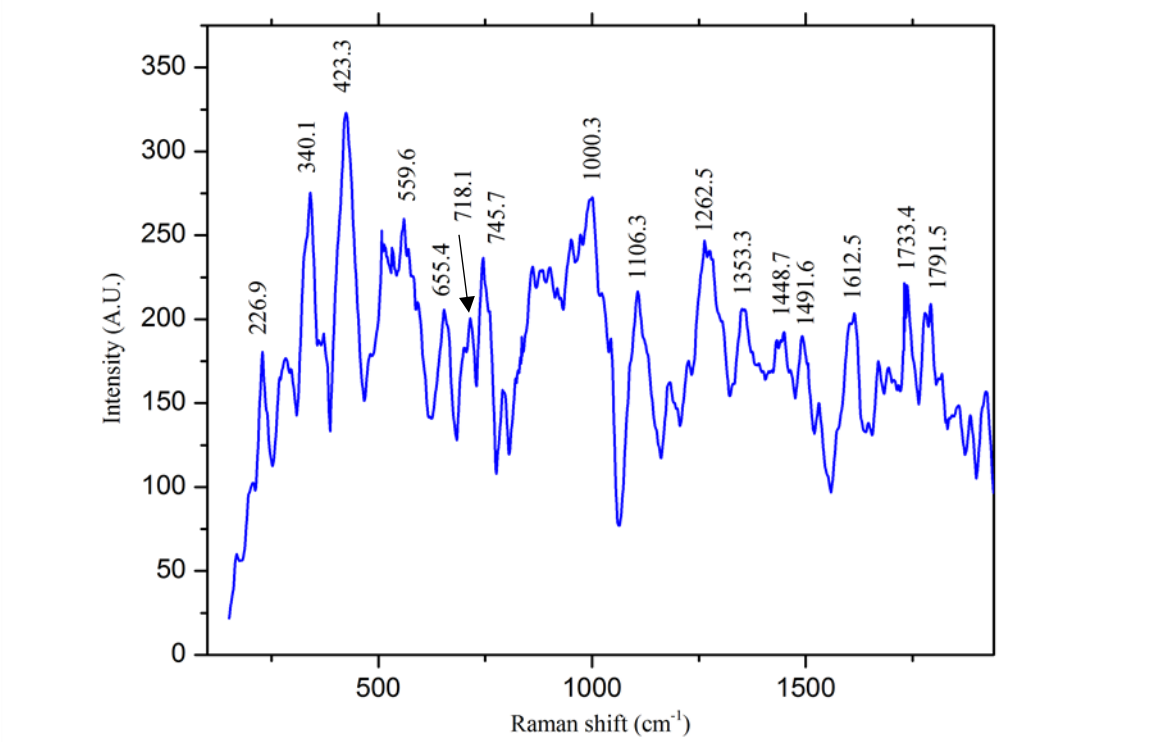

Figure 6.3: Raman spectra of powered apo-ferritin in water after incubation. No filter was used during laser excitation, and water evaporated from the sample.

Both laser settings resulted similar spectra with very close positions of peaks. The shifts in the Raman bands are only minor. Raman bands assigned to CH_2 deformations and CH, CH_2, CH_3 bending were observed in all the spectra that I obtained. In ferritin solution, the band appeared at 1435.4 cm^{-1}, in apo-ferritin at 1444.7 cm^{-1}, and in incubated apo-ferritin at 1448.7 cm^{-1} and 1438.9 cm^{-1} respectively without filter and with D1 filter blocking half of the laser power. I also observed the Phe and aromatic ring vibration's characteristic peak at slightly different positions ranging from 1602 cm^{-1} to 1614 cm^{-1}in the four samples. While using a filter for incubated apoferritin, I have observed C=C, C=N, and C=O bond's vibration bands at 1880-1970 cm^{-1}. These peaks are not strong while using maximum laser power.

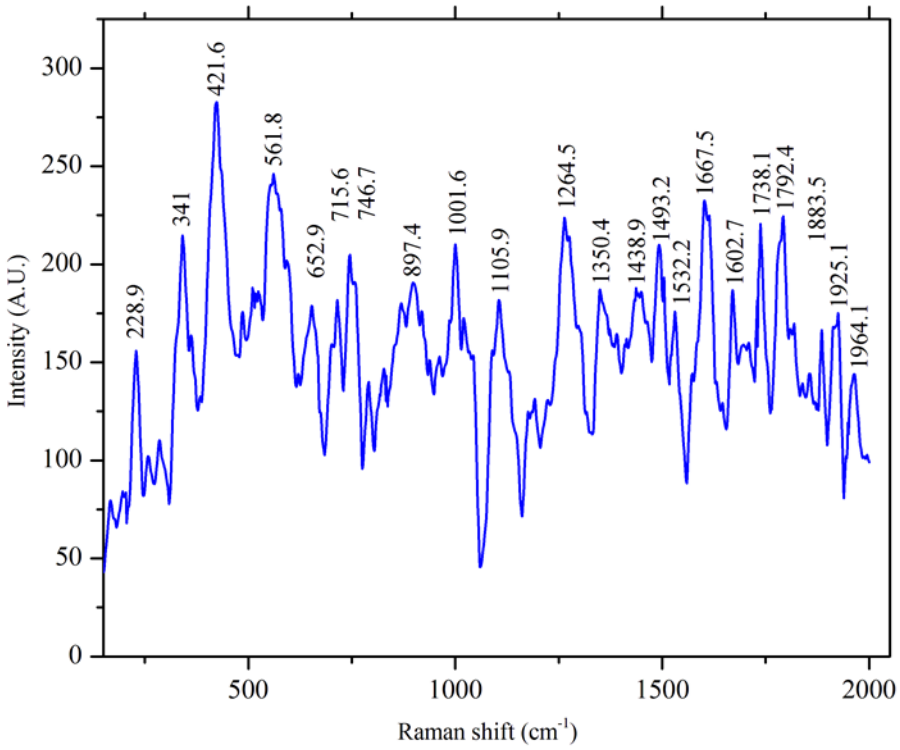

Figure 6.4: Raman spectra of powered apo-ferritin in water after incubation. A 50% filter was used during laser excitation, and water did not evaporate.

The positions and intensities of the three low-energy bands attributed to iron compounds are of special interest. In all cases, these bands experience an increase in intensity with the Raman shift. In ferritin solution, I observe the peaks at 230.4 cm^{-1}, 342.9 cm^{-1}, and 420.8 cm^{-1}. The peak positions are slightly different in powdered ferritin, where they are observed at 228.6 cm^{-1}, 341.4 cm^{-1}, and 424.8 cm^{-1}. The incubated ferritin powder in solution shows the three peaks in almost similar positions. The first peak appears at 226.9 cm^{-1} in the spectra without any filter, and at 228.9 cm^{-1} in the spectra with a filter that reduces the power by 50%. The two other peaks appear at 340.1 cm^{-1} and

423.3 cm^{-1} in the spectra without filter. Applying the filter results in the peaks appearing at 341 cm^{-1} and 421.6 cm^{-1}.

6.2. Raman Characterization Of Mohr's Salt

Mohr's salt (Ammonium iron (II) sulfate hexahydrate) is a common laboratory source of iron ions. Raman spectroscopy of Mohr's salt was performed in order to clarify, whether the three low-shift bands that were observed in different ferritin samples indeed should be attributed to iron ions' bonds with other compounds.

The experiment on Mohr's salt was done in two ways. In one setup, I used the powdered Mohr's salt on a Si substrate, and exposed the sample directly to the laser in order to acquire the Raman spectrum. In another setup, the Mohr's salt was incubated in Petri dish for about 18 hours at room temperature, on a similar Si substrate.

Figure 6.5 depicts a Raman spectrum of powdered Mohr's salt, and Figure 6.6 shows a Raman spectrum of incubated Mohr's salt solution. The spectrum of powder Mohr's salt exhibits three distinct low-shift bands at 191.9 cm^{-1}, 326.05 cm^{-1}, and 472.09 cm^{-1}, as shown in Figure 6.5. The incubated Mohr's salt solution shows three low-shift bands as well, at 183.23 cm^{-1}, 318.2 cm^{-1}, and 462.62 cm^{-1}. Thus, after incubation in water the bands are observed at lower Raman shifts.

I expect that the described bands originate from Fe-O bond vibrations. Iron oxides are known to produce low-shift Raman bands below 600 cm^{-1}.[113–115] For example, exposure of Fe_3O_4 to a 514.5 nm laser light yields a peak[116] at 474 cm^{-1}. In my experiments, I observe a very close peak at 472.09 cm^{-1} (Figure 6.5) and 462.62 cm^{-1} (Figure 6.6), in both setups.

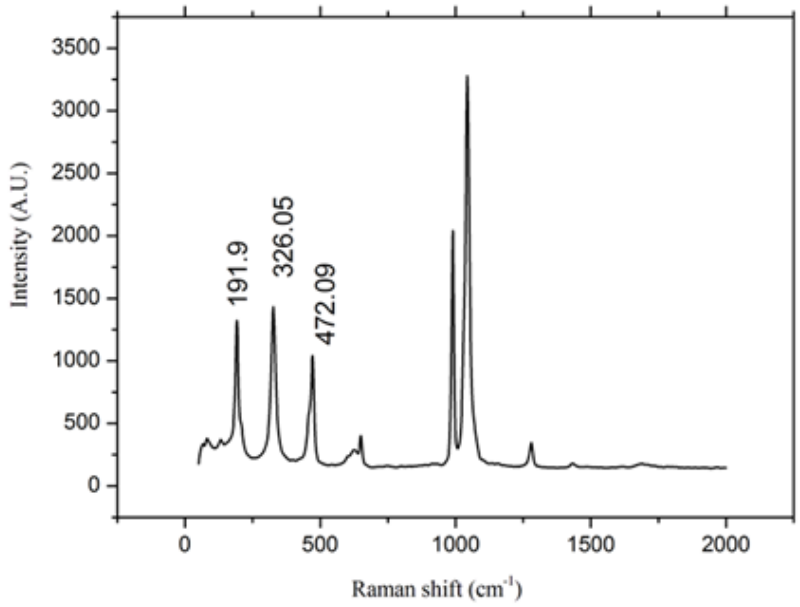

Figure 6.5: Raman spectra of Mohr's salt on Si substrate.

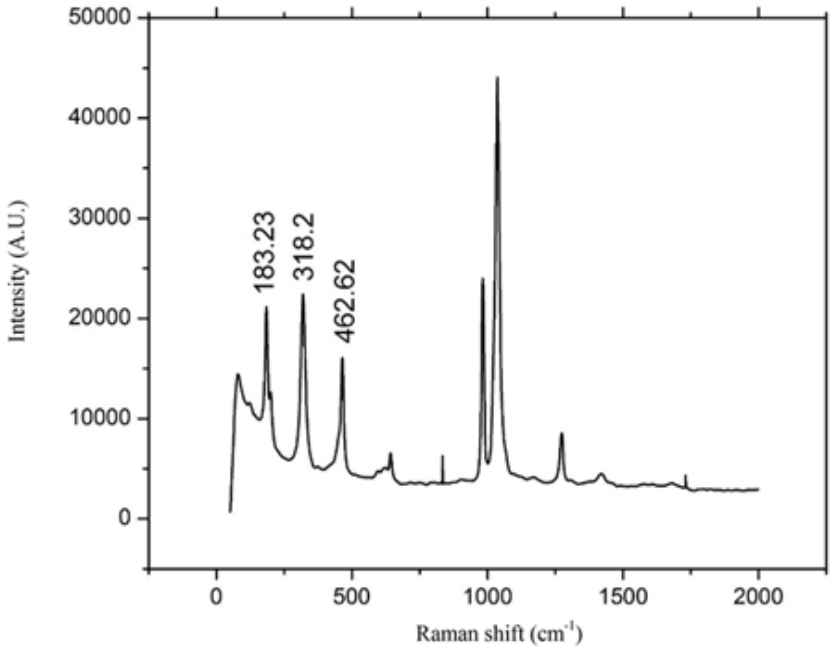

Figure 6.6: Raman spectrum of Mohr salt incubated in HPLC DI water on Si substrate.

Overall, these experiments indicate that indeed iron ions may produce thee strong, Raman bands in the low-shift region below 500 cm^{-1}. Specific positions of these bands may be influenced by presence of water, and other details of interactions of the ions with their surroundings.

6.3. Tentative SERS Characterization Of Ferritin

I did tentative proof-of-principle experiments on surface-enhanced Raman spectroscopy (SERS) of ferritin solution. For this purpose, I added a solution containing colloidal Au nanoparticles to my ferritin sample.

The 80 nm- sized Au nanoparticles were citrate-stabilized. Citrate anions form a negatively charged shell around each Au nanoparticle, preventing coalescence of the particles. Figure 6.7 represents a Raman spectrum of Au nanoparticles' solution on a silicon substrate for a reference. The spectrum exhibits several relatively weak bands at 416-431 cm^{-1}, 748.9 cm^{-1}, 826-880.9 cm^{-1}, 956.7 cm^{-1}, 1258.9 cm^{-1}, 1644.9 cm^{-1}, and 1825.9 cm^{-1}, which I attribute primarily to citrate shells of Au nanoparticles. A strong band at 520 cm^{-1} originates from silicon substrate.

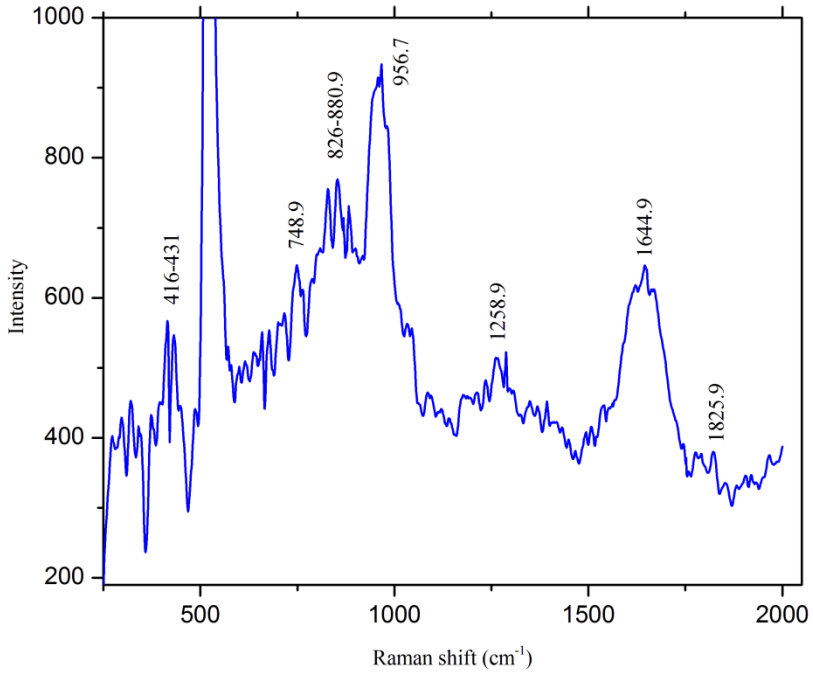

Figure 6.7: Raman spectrum of citrate-stabilized Au nanoparticles' solution on a Si substrate.

Preparation of a mixture of ferritin and Au nanoparticles solution was very simple. Using a micropipette, a droplet of ferritin solution was deposited on the surface of a substrate; then a droplet of citrate-stabilized Au nanoparticles in a PBS solution was deposited onto the same region. The ratio of ferritin solution and Au NPs solution was 1:2. For substrates, Au coated glass slides were used in these experiments.

Figure 6.8. shows raw Raman spectra of two samples, a regular ferritin solution, and a mixture of ferritin solution with Au nanoparticles. A pronounced enhancement of inelastic scattering is evident in the 50-1000 cm^{-1} range.

Figure 6.9 shows a background-subtracted Raman spectrum of ferritin solution with Au nanoparticles. The band assignments from table 6.1 are applicable to this graph

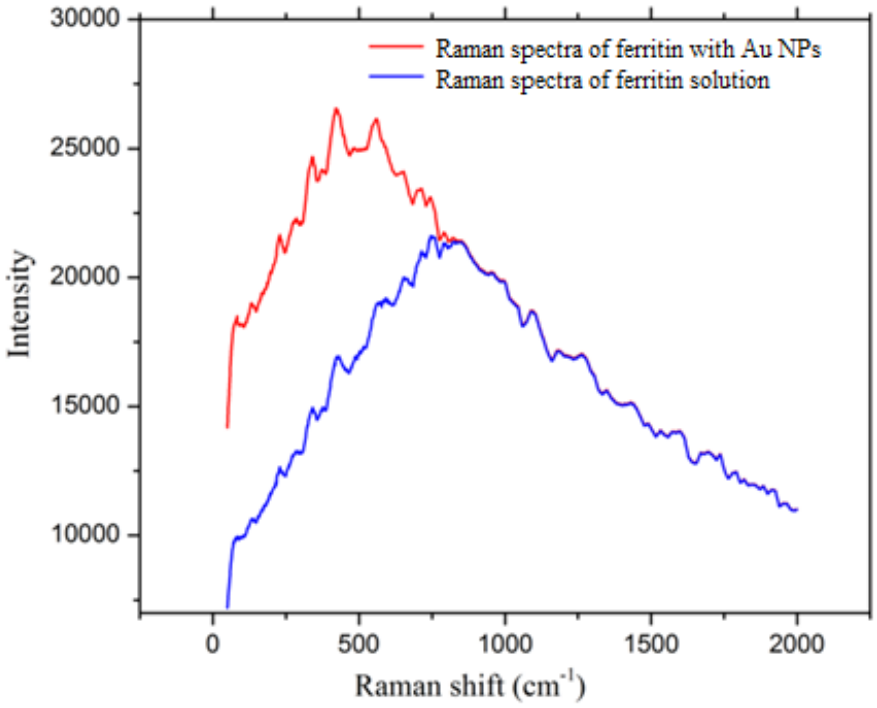

Figure 6.8: Raw Raman spectra of ferritin solution with Au nanoparticles (red line), and of regular ferritin solution without nanoparticles (blue line) on Au coated glass substrate. These spectra were not background-subtracted.

as well. I can see a significant enhancement of the signal in the low-shift part of the spectrum below 750 cm^{-1}. The three peaks that I tentatively attribute to iron ion compounds have undergone the strongest enhancement. There is a small peak at 270.5 cm^{-1}, presumably originating from Au nanoparticles, as in Figure 6.7, smaller peaks are visible around a 250 cm^{-1} region. However, all major peaks from 550 cm^{-1} to 1440 cm^{-1} and from 1600 cm^{-1} to 1880 cm^{-1} are very closely positioned to their counterparts in the Raman spectra of ferritin solution, ferritin powder, and incubated ferritin samples from Section 6.1.

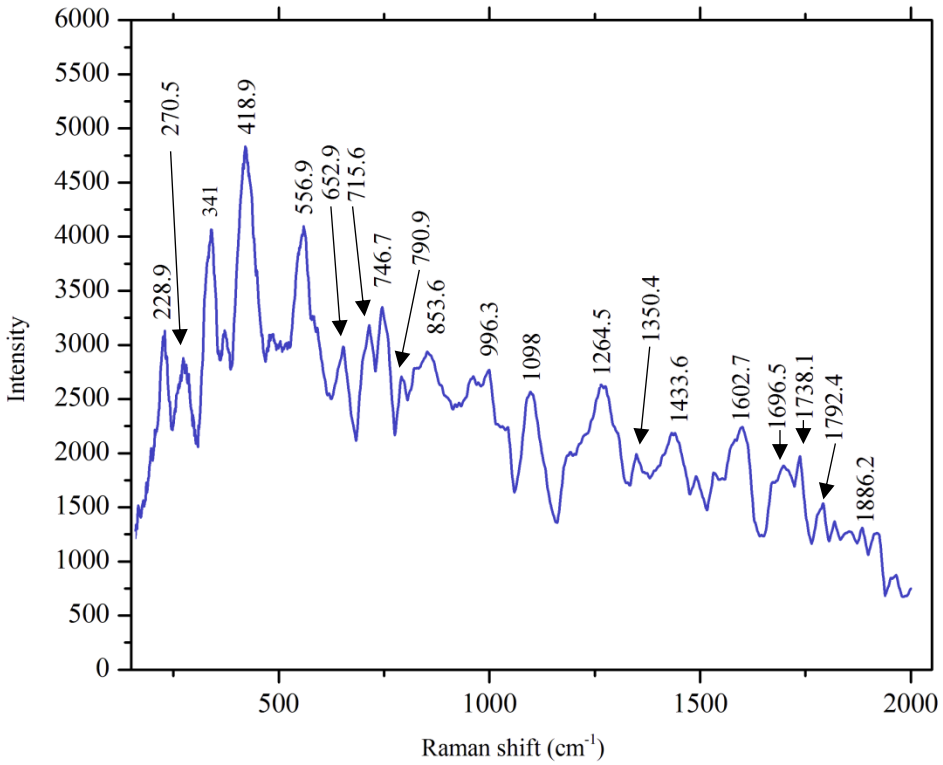

Figure 6.9: Background-subtracted Raman spectrum of ferritin solution containing Au nanoparticles.

CHAPTER 7: DISCUSSION

The Raman spectra of ferritin solution acquired in my experiments exhibit three distinct bands, at 230.4 cm^{-1}, 342.9 cm^{-1}, and 420.8 cm^{-1}. These bands are tentatively attributed to vibrations of iron ions containing compounds. In iron-loaded ferritin, vibrations of Fe–O bonds in ferrihydrite nanoparticles are a natural explanation. My Raman spectrum of Mohr's salt also contain three low-energy bands in the same region between approximately 180 cm^{-1} and 480 cm^{-1}. This supports my interpretation of the three distinct peaks in ferritin as originating from bonds of iron ions. Interestingly, in my SERS characterization of ferritin solution containing 80 nm Au nanoparticles, I achieved a significant enhancement of the iron-associated Raman bands. This indicates a strong potential of SERS as a method of investigating iron-loaded ferritin.

Surprisingly, the three characteristic bands were also present in Raman spectrum of apo-ferritin that does not contain ferrihydrite nanoparticles. The bands were observed in dry apo-ferritin powder, as well as after incubation of the powder in water.

The computational part of my work addresses the mechanism of transit of iron ions in and out of the ferritin's cage. my simulations indicate that ions located either side of ferritin's three-fold channel quickly enter into the channel in less than 2 ns, due to electrostatic attraction of negatively charged regions around the channel. In simulations with iron ions positioned on the outer side of the channel, the second and in one case, even the third ion entered the channel in the course of only 20 ns. These other ions seem to expel the first ion out of the channel by electrostatic repulsion. In two simulations out of the three, the first ion exited from the channel due to repelling action of another iron ion. In simulations with ions added on the inner side of the channel, one ion entered the

channel and remained there. The second ion approached closely, but did not enter the channel. In one trajectory, two ions approached the channel from inside. However, the second and third ions did not enter the channel, and the first ion did not exit in any of the three simulations with ions positioned inside.

In all cases, ions that enter the three-fold channel of ferritin are found in a stable position, and may remain there for a long time. From electrostatic potential analysis, I saw that three-fold channels are negatively charged. The positively charged iron ion is stable surrounded by acidic groups from ferritin's side chains. For an iron ion to exit from the channel, it needs a repulsion from second or possibly even third ion. In the absence of the other ions in the channel, the first ion does not exit.

The described computational results help explain why, in my experiments, apo-ferritin exhibits three distinct low-shift Raman bands, which are attributable to iron compounds. I hypothesize that these bands may originate from iron ions caught in, or closely positioned to three-fold channels of apo-ferritin. my molecular dynamics results indicate that iron ions in the channel are stable and can remain there for a significant time.

CHAPTER 8: CONCLUSIONS AND FUTURE WORK

8.1. Conclusions

An important cage protein, ferritin, has been investigated both computationally and experimentally. The following conclusions can be drawn.

- Results of my molecular dynamics simulations suggest that positively charged iron ions enter the three-fold channel of ferritin spontaneously, driven by attraction of negatively charged regions around the channel. A second ion, and sometimes more, were found to approach the channel. Some of these other ions entered the channel, following the first ion.
- In case of iron ions added outside of the channel, exit of the ion from the inner opening of the channel was observed. The second ion repeals the first ion toward its complete expulsion from the channel. The effect of the second ion is critical for the expulsion of the first one.
- During their travel through the channel, iron ions remain surrounded by water solvation shells. The first solvation shell is very stable, and the second one undergoes only minor changes.
- Ion travelling through the channel are found in close proximity of carboxylate groups from Glu130 residues in the channel area, which attract the ions electrostatically. Mediation through water molecules seems to play an important role in this interaction.
- Without expulsion by a second ion, the first ion would remain in the channel.

- In my experimental work, Raman spectra of iron-loaded ferritin solution were obtained. The spectra contain three low-shift Raman bands, which have been attributed to vibrations of bonds in iron containing compounds.
- Raman spectra of apo-ferritin also exhibited similar low-shift bands. Based on the results of MD simulations, these bands are thought to originate from interactions of iron ions in ferritin's channels.
- Raman characterization of ferritin solution with the addition of colloidal Au nanoparticles has demonstrated a pronounced Raman signal enhancement in the low-shift area, promising a strong potential of SERS for characterization of ferritin.

8.2. Future Work

Investigating interactions of iron ions inside ferritin's globule is important to elucidate details of ferritin functionality. The function of iron storage and release of ferritin can be extended to different nanoparticles storage and release, employing modified ferritin-like cage proteins. Molecular dynamics case studies of such proteins will also be useful.

For future works, the author suggests extending molecular dynamics simulations to even longer time. Also, adding more ions in simulation boxes, while balancing the charge though negative counterions, may allow observing more than two ions entering in the channel. Increasing the simulation box size would also be required to decrease the number of ions per unit volume, in order to observe a complete ion expulsion from the channel.

Raman characterization, on the other hand, could be extended to different modified ferritins, such as PDB ID 5CZU, which can be synthesized and undergo Raman or SERS characterization. Modified ferritins may have improved engineered functionalities. For instance, 5CZU has Sulphur containing side chains in three residues near the three-fold channel on the outside of the cage. These Sulphur groups may be used to bind ferritin to gold nanoparticles, enabling an efficient SERS enhancement is achieved in the region of three-fold channel.

Many applications that use nanoparticles, such as for example cancer therapies, require transport of caged NPs, making detailed vibrational characterization and molecular dynamics studies of ferritin and ferritin-like proteins very much important for future advancement of materials science.

REFERENCES

1. Zazo, H., Colino, C. I. & Lanao, J. M. Current applications of nanoparticles in infectious diseases. *Journal of Controlled Release* **224,** 86–102 (2016).

2. Romo-Herrera, J. M. *et al.* A study of the depth and size of concave cube Au nanoparticles as highly sensitive SERS probes. *Nanoscale* **8,** 7326–7333 (2016).

3. Oberdörster, G., Oberdörster, E. & Oberdörster, J. Nanotoxicology: An Emerging Discipline Evolving from Studies of Ultrafine Particles. *Environ. Health Perspect.* **113,** 823–839 (2005).

4. Lacave, J. M. *et al.* Effects of metal-bearing nanoparticles (Ag, Au, CdS, ZnO, SiO 2) on developing zebrafish embryos. *Nanotechnology* **27,** 325102 (2016).

5. Salata, O. Applications of nanoparticles in biology and medicine. *J. Nanobiotechnology* **2,** 3 (2004).

6. Talapin, D. V. & Shevchenko, E. V. Introduction: Nanoparticle chemistry. *Chem. Rev.* **116,** 10343–10345 (2016).

7. Hoecker, C., Smail, F., Bajada, M., Pick, M. & Boies, A. Catalyst nanoparticle growth dynamics and their influence on product morphology in a CVD process for continuous carbon nanotube synthesis. *Carbon N. Y.* **96,** 116–124 (2016).

8. Park, J. *et al.* Cooperative nanomaterial system to sensitize , target , and treat tumors. **107,** (2010).

9. Desiraju, G. R. The Raman Effect. *Nat. India* 1–3 (2008). doi:10.1038/nindia.2008.302

10. Butler, H. J. *et al.* Using Raman spectroscopy to characterize biological materials. *Nat. Protoc.* **11,** 664–687 (2016).

11. Zrimsek, A. B. *et al.* Single-Molecule Chemistry with Surface- and Tip-Enhanced Raman Spectroscopy. *Chem. Rev.* acs.chemrev.6b00552 (2016). doi:10.1021/acs.chemrev.6b00552

12. Kneipp, K., Kneipp, H., Itzkan, I., Dasari, R. R. & Feld, M. S. Surface-Enhanced Raman Scattering and Biophysics. *J. Phys. Condens. Matter Matter* **14,** R597–R624 (2002).

13. Stiles, P. L., Dieringer, J. a, Shah, N. C. & Van Duyne, R. P. Surface-enhanced Raman spectroscopy. *Annu. Rev. Anal. Chem. (Palo Alto. Calif).* **1,** 601–626 (2008).

14. Sergiienko, S., Moor, K., Gudun, K., Elemessova, Z. & Bukasov, R. Nanoparticle-nanoparticle vs nanoparticle-substrate hot spot contributions to SERS signal: studying Raman labelled monomers, dimers and trimers. *Phys. Chem. Chem. Phys.* **19,** 4478–4487 (2016).

15. Wustholz, K. L. *et al.* Structure-activity relationships in gold nanoparticle dimers and trimers for surface-enhanced raman spectroscopy. *J. Am. Chem. Soc.* **132,** 10903–10910 (2010).

16. Xu, L. *et al.* Label-Free Detection of Native Proteins by Surface-Enhanced Raman Spectroscopy Using Iodide-Modified Nanoparticles. *Anal. Chem.* **86,** 2238–2245 (2014).

17. Han, X. X., Huang, G. G., Zhao, B. & Ozaki, Y. Label-Free Highly Sensitive Detection of Proteins in Aqueous Solutions Using Surface-Enhanced Raman Scattering. *Anal. Chem.* **81,** 3329–3333 (2009).

18. Huang, G. G., Han, X. X., Hossain, M. K. & Osaki, Y. Development of a Heat-Induced Surface-Enhanced Raman Scattering Sensing Method for Rapid Detection of Glutathione in Aqueous Solutions. *Anal. Chem.* **81,** 5881–5888 (2009).

19. Kahraman, M., Balz, B. N. & Wachsmann-Hogiu, S. Hydrophobicity-driven self-assembly of protein and silver nanoparticles for protein detection using surface-enhanced Raman scattering. *Analyst* **138,** 2906–13 (2013).

20. Israelsen, N. D., Hanson, C. & Vargis, E. Nanoparticle Properties and Synthesis Effects on Surface-Enhanced Raman Scattering Enhancement Factor: An Introduction. *Sci. World J.* **2015,** 1–12 (2015).

21. Lyandres, O. *et al.* Progress toward an in vivo surface-enhanced Raman spectroscopy glucose sensor. *Diabetes Technol. Ther.* **10,** 257–65 (2008).

22. Yonzon, C. R., Haynes, C. L., Zhang, X., Walsh, J. T. & Van Duyne, R. P. A Glucose Biosensor Based on Surface-Enhanced Raman Scattering: Improved Partition Layer, Temporal Stability, Reversibility, and Resistance to Serum Protein Interference. *Anal. Chem.* **76,** 78–85 (2004).

23. Dendisova-Vyskovska, M., Broncova, G., Clupek, M., Prokopec, V. & Matejka, P. In situ SERS spectroelectrochemical analysis of antioxidants deposited on copper substrates: What is the effect of applied potential on sorption behavior? *Spectrochim. Acta - Part A Mol. Biomol. Spectrosc.* **99,** 196–204 (2012).

24. Podstawka, E., Ozaki, Y. & Proniewicz, L. M. Part III: Surface-enhanced raman scattering of amino acids and their homodipeptide monolayers deposited onto colloidal gold surface. *Appl. Spectrosc.* **59,** 1516–1526 (2005).

25. Barhoumi, A., Zhang, D., Tam, F. & Halas, N. J. Surface-enhanced Raman spectroscopy of DNA. *J. Am. ...* **130,** 5523–9 (2008).

26. Cui, Y. *et al.* Au@organosilica multifunctional nanoparticles for the multimodal imaging. *Chem. Sci.* **2,** 1463–1469 (2011).

27. Qian, X. *et al.* In vivo tumor targeting and spectroscopic detection with surface-enhanced Raman nanoparticle tags. *Nat. Biotechnol.* **26,** 83–90 (2008).

28. Pallaoro, A., Hoonejani, M. R., Braun, G. B., Meinhart, C. D. & Moskovits, M. Rapid identification by surface-enhanced raman spectroscopy of cancer cells at

low concentrations flowing in a microfluidic channel. *ACS Nano* **9,** 4328–4336 (2015).

29. Lin, D. *et al.* Label-free detection of blood plasma using silver nanoparticle based surface-enhanced Raman spectroscopy for esophageal cancer screening. *J. Biomed. Nanotechnol.* **10,** 478–484 (2014).

30. Yang, J. *et al.* Surface-enhanced Raman spectroscopy based quantitative bioassay on aptamer-functionalized nanopillars using large-area Raman mapping. *ACS Nano* **7,** 5350–5359 (2013).

31. MaHam, A., Tang, Z., Wu, H., Wang, J. & Lin, Y. Protein-Based Nanomedicine Platforms for Drug Delivery. *Small* **5,** 1706–1721 (2009).

32. Bantz, K. C. *et al.* Recent progress in SERS biosensing. *Phys. Chem. Chem. Phys.* **13,** 11551–67 (2011).

33. Wang, Y., Lee, K. & Irudayaraj, J. SERS aptasensor from nanorod–nanoparticle junction for protein detection. *Chem. Commun.* **46,** 613–615 (2010).

34. Han, X. X., Zhao, B. & Ozaki, Y. Surface-enhanced Raman scattering for protein detection. *Analytical and Bioanalytical Chemistry* **394,** 1719–1727 (2009).

35. Hildebrandt, P. & Stockburger, M. Surface-enhanced resonance Raman spectroscopy of Rhodamine 6G adsorbed on colloidal silver. *J. Phys. Chem.* **88,** 5935–5944 (1984).

36. Xu, T. *et al.* Enhanced Raman scattering assisted by ultrahigh order modes of the double metal cladding waveguide. *Appl. Phys. Lett.* **105,** 163703 (2014).

37. Rodríguez-Torres, M. del P., Díaz-Torres, L. A. & Romero-Servin, S. Heparin assisted photochemical synthesis of gold nanoparticles and their performance as SERS substrates. *Int. J. Mol. Sci.* **15,** 19239–19252 (2014).

38. Rowland, C. E., Brown, C. W., Delehanty, J. B. & Medintz, I. L. Nanomaterial-based sensors for the detection of biological threat agents. *Mater. Today* **19,** 464–477 (2016).

39. Bell, S. E. J. & Sirimuthu, N. M. S. Surface-Enhanced Raman Spectroscopy (SERS) for Sub-Micromolar Detection of DNA/RNA Mononucleotides. *J. Am. Chem. Soc.* **128,** 15580–15581 (2006).

40. Pincella, F., Isozaki, K. & Miki, K. A visible light-driven plasmonic photocatalyst. *Light Sci. Appl.* **3,** e133 (2014).

41. Delga, A., Feist, J., Bravo-Abad, J. & Garcia-Vidal, F. J. Theory of strong coupling between quantum emitters and localized surface plasmons. *J. Opt.* **16,** 114018 (2014).

42. Guarrotxena, N. & Bazan, G. C. Antitags: SERS-encoded nanoparticle assemblies that enable single-spot multiplex protein detection. *Adv. Mater.* **26,** 1941–1946 (2014).

43. Han, X. X. *et al.* Protein-mediated sandwich strategy for surface-enhanced raman scattering: Application to versatile protein detection. *Anal. Chem.* **81,** 3350–3355 (2009).

44. Lim, D.-K. *et al.* Highly uniform and reproducible surface-enhanced Raman scattering from DNA-tailorable nanoparticles with 1-nm interior gap. *Nat. Nanotechnol.* **6,** 452–460 (2011).

45. Feng, M. & Tachikawa, H. Surface-enhanced resonance Raman spectroscopic characterization of the protein native structure. *J. Am. Chem. Soc.* **130,** 7443–7448 (2008).

46. Bernardi, R. C., Melo, M. C. R. & Schulten, K. Enhanced sampling techniques in molecular dynamics simulations of biological systems. *Biochim. Biophys. Acta* **1850,** 872–877 (2015).

47. Perilla, J. R. *et al.* Molecular dynamics simulations of large macromolecular complexes. *Current Opinion in Structural Biology* **31,** 64–74 (2015).

48. Malmstrom, R. D., Lee, C. T., Van Wart, A. T. & Amaro, R. E. Application of molecular-dynamics based markov state models to functional proteins. *J. Chem. Theory Comput.* **10,** 2648–2657 (2014).

49. Han, Y. & Elliott, J. Molecular dynamics simulations of the elastic properties of polymer/carbon nanotube composites. *Comput. Mater. Sci.* **39,** 315–323 (2007).

50. Karplus, M. & McCammon, J. A. Molecular dynamics simulations of biomolecules. *Nat. Struct. Biol.* **9,** 646–652 (2002).

51. MacKerell, A. D. & Banavali, N. K. All-atom empirical force field for nucleic acids: II. Application to molecular dynamics simulations of DNA and RNA in solution. *J. Comput. Chem.* **21,** 105–120 (2000).

52. Wilfred, B., Gunsteren, V. & Berendsen, C. Computer Simulation of Molecular Dynamics: Methodology, Applications, and Perspectives in Chemistry. *Anger,. Chem. lnr. Ed. Engl* **29,** 992–1023 (1990).

53. Sankey, O. F. & Niklewski, D. J. Ab initio multicenter tight-binding model for molecular-dynamics simulations and other applications in covalent systems. *Phys. Rev. B* **40,** 3979–3995 (1989).

54. Miao, Y. *et al.* Improved reweighting of accelerated molecular dynamics simulations for free energy calculation. *J. Chem. Theory Comput.* **10,** 2677–2689 (2014).

55. Simonson, T., Archontis, G. & Karplus, M. Free Energy Simulations Come of Age: Protein−Ligand Recognition. *Acc. Chem. Res.* **35,** 430–437 (2002).

56. Humphrey, W., Dalke, A. & Schulten, K. VMD: Visual molecular dynamics. *J. Mol. Graph.* **14,** 33–38 (1996).

57. Karplus, M. Molecular dynamics of biological macromolecules: A brief history

and perspective. in *Biopolymers* **68,** 350–358 (2003).

58. Kumar, A. & Purohit, R. Use of Long Term Molecular Dynamics Simulation in Predicting Cancer Associated SNPs. *PLoS Comput. Biol.* **10,** (2014).

59. Laghaei, R., Kowallis, W., Evans, D. G. & Coalson, R. D. Calculation of iron transport through human H-chain ferritin. *J. Phys. Chem. A* **118,** 7442–7453 (2014).

60. Chandramouli, B., Bernacchioni, C., Di Maio, D., Turano, P. & Brancato, G. Electrostatic and Structural Bases of Fe2+ Translocation Through Ferritin Channels. *J. Biol. Chem.* M116.748046- (2016). doi:10.1074/jbc.M116.748046

61. Laghaei, R., Evans, D. G. & Coalson, R. D. Metal binding sites of human H-chain ferritin and iron transport mechanism to the ferroxidase sites: A molecular dynamics simulation study. *Proteins Struct. Funct. Bioinforma.* **81,** 1042–1050 (2013).

62. Honarmand Ebrahimi, K., Hagedoorn, P.-L. & Hagen, W. R. Unity in the Biochemistry of the Iron-Storage Proteins Ferritin and Bacterioferritin. *Chem. Rev.* **115,** 295–326 (2015).

63. Nakajima, H. *et al.* Construction of an enterobactin analogue with symmetrically arranged monomer subunits of ferritin. *Chem. Commun.* **51,** 16609–16612 (2015).

64. Schrödinger, LLC. *The {PyMOL} Molecular Graphics System, Version~1.8*. (2015).

65. Jutz, G., van Rijn, P., Santos Miranda, B. & Böker, A. Ferritin: A Versatile Building Block for Bionanotechnology. *Chem. Rev.* **115,** 1653–1701 (2015).

66. MULLER, R. N. *et al.* RELAXATION BY METAL-CONTAINING NANOSYSTEMS. *Advances in Inorganic Chemistry* **57,** 239–292 (2006).

67. Schrödinger, LLC. *The {JyMOL} Molecular Graphics Development Component, Version~1.8*. (2015).

68. Kasyutich, O. *et al.* Silver Ion Incorporation and Nanoparticle Formation inside the Cavity of Pyrococcus furiosus Ferritin: Structural and Size-Distribution Analyses. *J. Am. Chem. Soc.* **132,** 3621–3627 (2010).

69. May, C. A. *et al.* The sedimentation properties of ferritins. New insights and analysis of methods of nanoparticle preparation. *Biochim. Biophys. Acta - Gen. Subj.* **1800,** 858–870 (2010).

70. Polanams, J., Ray, A. D. & Watt, R. K. Nanophase Iron Phosphate, Iron Arsenate, Iron Vanadate, and Iron Molybdate Minerals Synthesized within the Protein Cage of Ferritin. *Inorg. Chem.* **44,** 3203–3209 (2005).

71. Bedwell, G. J. *et al.* Selective Biotemplated Synthesis of TiO2 Inside a Protein Cage. *Biomacromolecules* **16,** 214–218 (2015).

72. Douglas, T. & Young, M. Host-guest encapsulation of materials by assembled

virus protein cages. *Nature* **393,** 152–155 (1998).

73. Kang, S. *et al.* Implementation of P22 Viral Capsids as Nanoplatforms. *Biomacromolecules* **11,** 2804–2809 (2010).

74. Steinmetz, N. F. Viral Nanoparticles in Drug Delivery and Imaging. *Mol. Pharm.* **10,** 1–2 (2013).

75. Molino, N. M. & Wang, S. W. Caged protein nanoparticles for drug delivery. *Curr. Opin. Biotechnol.* **28,** 75–82 (2014).

76. Farokhzad, O. C. & Langer, R. Impact of Nanotechnology on Drug Delivery. *ACS Nano* **3,** 16–20 (2009).

77. Wagner, V., Dullaart, A., Bock, A.-K. & Zweck, A. The emerging nanomedicine landscape. *Nat Biotech* **24,** 1211–1217 (2006).

78. Yildiz, I., Shukla, S. & Steinmetz, N. F. Applications of viral nanoparticles in medicine. *Curr. Opin. Biotechnol.* **22,** 901–908 (2011).

79. Uchida, M. *et al.* Biological Containers: Protein Cages as Multifunctional Nanoplatforms. *Adv. Mater.* **19,** 1025–1042 (2007).

80. Smith, M. T., Hawes, A. K. & Bundy, B. C. Reengineering viruses and virus-like particles through chemical functionalization strategies. *Curr. Opin. Biotechnol.* **24,** 620–626 (2013).

81. Aljabali, A. A. A., Shukla, S., Lomonossoff, G. P., Steinmetz, N. F. & Evans, D. J. CPMV-DOX Delivers. *Mol. Pharm.* **10,** 3–10 (2013).

82. Moon, H., Lee, J., Min, J. & Kang, S. Developing Genetically Engineered Encapsulin Protein Cage Nanoparticles as a Targeted Delivery Nanoplatform. *Biomacromolecules* **15,** 3794–3801 (2014).

83. Berendsen, H. J. C., van der Spoel, D. & van Drunen, R. GROMACS: A message-passing parallel molecular dynamics implementation. *Comput. Phys. Commun.* **91,** 43–56 (1995).

84. Lindahl, E., Hess, B. & Spoel, D. Van Der. GROMACS 3 . 0 : a package for molecular simulation and trajectory analysis. *J. Mol. Model.* 306–317 (2001). doi:10.1007/s008940100045

85. Van Der Spoel, D. *et al.* GROMACS: Fast, flexible, and free. *J. Comput. Chem.* **26,** 1701–1718 (2005).

86. Hess, B., Kutzner, C., van der Spoel, D. & Lindahl, E. GROMACS 4: Algorithms for Highly Efficient, Load-Balanced, and Scalable Molecular Simulation. *J. Chem. Theory Comput.* **4,** 435–447 (2008).

87. Pronk, S. *et al.* GROMACS 4.5: a high-throughput and highly parallel open source molecular simulation toolkit. *Bioinformatics* **29,** 845 (2013).

88. Páll, S., Abraham, M. J., Kutzner, C., Hess, B. & Lindahl, E. in (eds. Markidis, S.

& Laure, E.) 3–27 (Springer International Publishing, 2015). doi:10.1007/978-3-319-15976-8_1

89. Abraham, M. J. *et al.* Gromacs: High performance molecular simulations through multi-level parallelism from laptops to supercomputers. *SoftwareX* **1–2,** 19–25 (2015).

90. Van Gunsteren, F. W. *et al. Biomolecular Simulation: The GROMOS96 Manual and User Guide*. *Biomolecular Simulation: The GROMOS96 Manual and User Guide* (1996). doi:citeulike-article-id:8062915

91. Oostenbrink, C., Villa, A., Mark, A. E. & Van Gunsteren, W. F. A biomolecular force field based on the free enthalpy of hydration and solvation: The GROMOS force-field parameter sets 53A5 and 53A6. *J. Comput. Chem.* **25,** 1656–1676 (2004).

92. Jorgensen, W. L., Maxwell, D. S. & Tirado-Rives, J. Development and Testing of the OPLS All-Atom Force Field on Conformational Energetics and Properties of Organic Liquids. *J. Am. Chem. Soc.* **118,** 11225–11236 (1996).

93. Kaminski, G. A., Friesner, R. A., Tirado-Rives, J. & Jorgensen, W. L. Evaluation and Reparametrization of the OPLS-AA Force Field for Proteins via Comparison with Accurate Quantum Chemical Calculations on Peptides. *J. Phys. Chem. B* **105,** 6474–6487 (2001).

94. Brooks, B. R. *et al.* CHARMM: The biomolecular simulation program. *J. Comput. Chem.* **30,** 1545–1614 (2009).

95. Case, D. A. *et al.* The Amber biomolecular simulation programs. *J. Comput. Chem.* **26,** 1668–1688 (2005).

96. Hess, B., Spoel, D. van der & Lindahl, E. Gromacs User Manual. *Dep. Biophys. Chem. ...* 312 (2014). doi:10.1006/imms.1993.1022

97. Berendsen, H. J. C., Postma, J. P. M., van Gunsteren, W. F. & Hermans, J. in *Intermolecular Forces: Proceedings of the Fourteenth Jerusalem Symposium on Quantum Chemistry and Biochemistry Held in Jerusalem, Israel, April 13--16, 1981* (ed. Pullman, B.) 331–342 (Springer Netherlands, 1981). doi:10.1007/978-94-015-7658-1_21

98. Li, P., Roberts, B. P., Chakravorty, D. K. & Merz, K. M. Rational design of particle mesh ewald compatible lennard-jones parameters for +2 metal cations in explicit solvent. *J. Chem. Theory Comput.* **9,** 2733–2748 (2013).

99. Bussi, G., Donadio, D. & Parrinello, M. Canonical sampling through velocity rescaling. *J. Chem. Phys.* **126,** (2007).

100. Nosé, S. & Klein, M. L. Constant pressure molecular dynamics for molecular systems. *Mol. Phys.* **50,** 1055–1076 (1983).

101. Parrinello, M. & Rahman, A. Polymorphic transitions in single crystals: A new molecular dynamics method. *J. Appl. Phys.* **52,** 7182–7190 (1981).

102. Hess, B., Bekker, H., Berendsen, H. J. C. & Fraaije, J. G. E. M. LINCS: A Linear Constraint Solver for Molecular Simulations. *J. Comput. Chem* **18,** 18–1463 (1997).

103. Miyamoto, S. & Kollman, P. A. Settle: An analytical version of the SHAKE and RATTLE algorithm for rigid water models. *J. Comput. Chem.* **13,** 952–962 (1992).

104. Mathews, N. VMD User ' s Guide. *Methods* **51,** 1581 (2009).

105. Caddigan, E., Cohen, J., Gullingsrud, J. & Stone, J. VMD User's Guide. *Urbana* **51,** 61801 (2003).

106. Frishman, D. & Argos, P. Knowledge???based protein secondary structure assignment. *Proteins Struct. Funct. Bioinforma.* **23,** 566–579 (1995).

107. PDB2PQR Server. doi:http://nbcr-222.ucsd.edu/pdb2pqr_2.1.1/

108. Rygula, A. *et al.* Raman spectroscopy of proteins: A review. *Journal of Raman Spectroscopy* **44,** 1061–1076 (2013).

109. Kurouski, D., Postiglione, T., Deckert-Gaudig, T., Deckert, V. & Lednev, I. K. Amide I vibrational mode suppression in surface (SERS) and tip (TERS) enhanced Raman spectra of protein specimens. *Analyst* **138,** 1665 (2013).

110. Barth, A. Infrared spectroscopy of proteins. *Biochimica et Biophysica Acta - Bioenergetics* **1767,** 1073–1101 (2007).

111. Tuma, R. Raman spectroscopy of proteins: from peptides to large assemblies. *J. Raman Spectrosc.* **36,** 307–319 (2005).

112. Barth, A. & Zscherp, C. What vibrations tell about proteins. *Q. Rev. Biophys.* **35,** S0033583502003815 (2002).

113. Fan, F., Feng, Z. & Li, C. UV Raman Spectroscopic Studies on Active Sites and Synthesis Mechanisms of Transition Metal-Containing Microporous and Mesoporous Materials. *Acc. Chem. Res.* **43,** 378–387 (2010).

114. Chourpa, I. *et al.* Molecular composition of iron oxide nanoparticles{,} precursors for magnetic drug targeting{,} as characterized by confocal Raman microspectroscopy. *Analyst* **130,** 1395–1403 (2005).

115. Li, C. Identifying the isolated transition metal ions/oxides in molecular sieves and on oxide supports by UV resonance Raman spectroscopy. *J. Catal.* **216,** 203–212 (2003).

116. Mitchell, E. *et al.* Probing on the hydrothermally synthesized iron oxide nanoparticles for ultra-capacitor applications. *Powder Technol.* **272,** 295–299 (2015).